NAVAL POSTGRADUATE SCHOOL

MONTEREY, CALIFORNIA

THESIS

IMPROVED BEAM JITTER CONTROL METHODS FOR HIGH ENERGY LASER SYSTEMS

by

Duane C. Frist

December 2009

Thesis Advisor:	Brij Agrawal
Co-Advisor:	Jae-Jun Kim

Approved for public release; distribution is unlimited

REPORT DOCUMENTATION PAGE		*Form Approved OMB No. 0704-0188*

Public reporting burden for this collection of information is estimated to average 1 hour per response, including the time for reviewing instruction, searching existing data sources, gathering and maintaining the data needed, and completing and reviewing the collection of information. Send comments regarding this burden estimate or any other aspect of this collection of information, including suggestions for reducing this burden, to Washington headquarters Services, Directorate for Information Operations and Reports, 1215 Jefferson Davis Highway, Suite 1204, Arlington, VA 22202-4302, and to the Office of Management and Budget, Paperwork Reduction Project (0704-0188) Washington DC 20503.

1. AGENCY USE ONLY *(Leave blank)*	2. REPORT DATE December 2009	3. REPORT TYPE AND DATES COVERED Master's Thesis	
4. TITLE AND SUBTITLE Improved Beam Jitter Control Methods for High Energy Laser Systems		**5. FUNDING NUMBERS**	
6. AUTHOR(S) Duane C. Frist			
7. PERFORMING ORGANIZATION NAME(S) AND ADDRESS(ES) Naval Postgraduate School Monterey, CA 93943-5000		**8. PERFORMING ORGANIZATION REPORT NUMBER**	
9. SPONSORING /MONITORING AGENCY NAME(S) AND ADDRESS(ES) N/A		**10. SPONSORING/MONITORING AGENCY REPORT NUMBER**	

11. SUPPLEMENTARY NOTES The views expressed in this thesis are those of the author and do not reflect the official policy or position of the Department of Defense or the U.S. Government.

12a. DISTRIBUTION / AVAILABILITY STATEMENT Approved for public release; distribution is unlimited	12b. DISTRIBUTION CODE

13. ABSTRACT (maximum 200 words)

The objective of this research was to develop beam jitter control methods for a High Energy Laser (HEL) testbed. The first step was to characterize the new HEL testbed at NPS. This included determination of natural frequencies and component models which were used to create a Matlab/Simulink model of the testbed.

Adaptive filters using Filtered-X Least Mean Squares (FX-LMS) and Filtered-X Recursive Least Square (FX-RLS) were then implemented. Disturbance sources included narrowband mechanical vibration of the optical bench as well as broadband atmospheric turbulence (simulation only). A feedback controller with adaptive filter (or feedback-type adaptive filter) was applied to a multi-rate video tracking loop, which required precise plant identification to prevent instabilities. A strapdown type Inertial Reference Unit (IRU) system was investigated using a reference laser, Position Sensing Device (PSD), Fiber Optic Gyro (FOG), and Fast Steering Mirror (FSM). The controller of the strapdown type IRU system consisted of a feedforward gyro signal in parallel with a feedback PSD signal. A Video tracking control system was simulated and tested on the HEL testbed. The IRU strapdown controller was simulated and preliminary tests conducted. Simulation and experimental results demonstrated superior performance over classical control methods.

14. SUBJECT TERMS High energy laser (HEL), Beam Control, Fast Steering Mirror (FSM), Two Axis Gimbal, Stabilization, Video Tracking, Feedforward Control, Adaptive Filter			**15. NUMBER OF PAGES** 89
			16. PRICE CODE
17. SECURITY CLASSIFICATION OF REPORT Unclassified	**18. SECURITY CLASSIFICATION OF THIS PAGE** Unclassified	**19. SECURITY CLASSIFICATION OF ABSTRACT** Unclassified	**20. LIMITATION OF ABSTRACT** UU

NSN 7540-01-280-5500

Standard Form 298 (Rev. 2-89)
Prescribed by ANSI Std. 239-18

i

THIS PAGE INTENTIONALLY LEFT BLANK

IMPROVED BEAM JITTER CONTROL METHODS FOR HIGH ENERGY LASER SYSTEMS

Duane C. Frist
Lieutenant Commander, United States Navy
B.S., Virginia Polytechnic Institute and State University, 1995

Submitted in partial fulfillment of the
requirements for the degree of

MASTER OF SCIENCE IN ASTRONAUTICAL ENGINEERING

from the

NAVAL POSTGRADUATE SCHOOL
December 2009

Author: Duane C. Frist

Approved by: Dr. Brij Agrawal
                 Thesis Advisor

                 Dr. Jae Jun Kim
                 Co-Advisor

                 Dr. Knox T. Millsaps
                 Chairman, Department of Mechanical and Astronautical
                 Engineering

THIS PAGE INTENTIONALLY LEFT BLANK

ABSTRACT

The objective of this research was to develop beam jitter control methods for a High Energy Laser (HEL) testbed. The first step was to characterize the new HEL testbed at NPS. This included determination of natural frequencies and component models which were used to create a Matlab/Simulink model of the testbed.

Adaptive filters using Filtered-X Least Mean Squares (FX-LMS) and Filtered-X Recursive Least Square (FX-RLS) were then implemented. Disturbance sources included narrowband mechanical vibration of the optical bench as well as broadband atmospheric turbulence (simulation only). A feedback controller with adaptive filter (or feedback-type adaptive filter) was applied to a multi-rate video tracking loop, which required precise plant identification to prevent instabilities. A strapdown type Inertial Reference Unit (IRU) system was investigated using a reference laser, Position Sensing Device (PSD), Fiber Optic Gyro (FOG), and Fast Steering Mirror (FSM). The controller of the strapdown type IRU system consisted of a feedforward gyro signal in parallel with a feedback PSD signal. A Video tracking control system was simulated and tested on the HEL testbed. The IRU strapdown controller was simulated and preliminary tests conducted. Simulation and experimental results demonstrated superior performance over classical control methods.

THIS PAGE INTENTIONALLY LEFT BLANK

TABLE OF CONTENTS

LIST OF FIGURES

LIST OF TABLES

THIS PAGE INTENTIONALLY LEFT BLANK

LIST OF ACRONYMS AND ABBREVIATIONS

ABL	Airborne Laser
ATL	Airborne Tactical Laser
COIL	Chemical Oxygen Iodine Laser
FIR	Finite Infinite Response
FOG	Fiber Optic Gyro
FSM	Fast Steering Mirror
FX-LMS	Filtered-X Least Mean Squares
FX-RLS	Filtered-X Recursive Least Square
HEL	High Energy Laser
JCT	Jitter Control Testbed
IRU	Inertial Reference Unit
LOS	Line of Site
LMS	Least Mean Squares
LPF	Low Pass Filter
MDA	Missile Defense Agency
NFOV	Narrow Field of View
PI	Proportional plus Integral
PSD	Position Sensing Device
RLS	Recursive Lease Squares
SOCOM	Special Operations Command
TBM	Theatre Ballistic Missile
THEL	Tactical High Energy Laser
WFOV	Wide Field of View

THIS PAGE INTENTIONALLY LEFT BLANK

ACKNOWLEDGMENTS

THIS PAGE INTENTIONALLY LEFT BLANK

I. INTRODUCTION

A. MOTIVATION

High energy laser (HEL) weapons are ready for some of the most challenging military applications in future battle fields since speed of light delivery enables the war fighter to engage very distant targets immediately. The issues of the technology on HEL systems include various types of high energy laser devices, beam control systems, atmospheric propagation, and target lethality issues. Among them, precision pointing of laser beam and high-bandwidth rejection of jitters produced by platform vibrations are the key technologies in the emerging fields of laser communications and HEL systems.

Optical beam control describes the centroid shifting of a laser on the target, and is a concern of engineers and scientists working with lasers and electro optical systems. Platform motion and optical component motion causes optical jitter, resulting in poor pointing accuracy, and blurred images. Even small level relative motion between mirrors and lenses can degrade the performance of precision pointing systems. Sources contributing to optical jitter include thermal effects, mechanical vibration, acoustics, static and dynamic loading, and heating and cooling systems.

The NPS HEL testbed has been developed to support research environments on the precision beam control technology including acquisition, tracking, and pointing. The testbed incorporates an optical table, two axis gimbal, high speed computers, and a variety of servo components, sensors, optical components, and software. This thesis describes the development of several jitter control methods and their implementation on the HEL testbed.

B. THESIS OVERVIEW

Chapter II provides background information relevant to this thesis, including information on HEL systems, beam control and IRUs.

Chapter III summarizes the HEL testbed here at NPS, including mathematical models and simulations.

Chapter IV provides an overview of the various control algorithms applied to the HEL testbed.

Chapter V describes experimental results.

II. BACKGROUND INFORMATION

There are three major areas that provide the necessary background for this thesis, those being high energy laser (HEL) systems, beam control methods—to include adaptive control theory, and finally inertial reference units (IRU). In many ways, these areas are related and depend upon one another for the entire system to work properly. Below is a brief synopsis of these areas.

A. HIGH ENERGY LASER SYSTEMS

Military interest in HEL systems begin shortly after the invention of the laser in the early 1960s. It is easy to understand such interest, what military would not desire the ability to attack an enemy at light speed, incinerating a target with a massive burst of photon energy? To date, three major demonstration programs in the field of directed energy have been undertaken. The first is the Army's Tactical High Energy Laser (THEL). This was a megawatt class chemical laser using deuterium fluoride. The THEL program proved the viability of HEL systems by successfully engaging and destroying several Katyusha rockets. Engagement ranges were on the order of several kilometers [1].

Currently, the DOD is developing two airborne HEL systems, the Advanced Tactical Laser (ATL), and the Airborne Laser (ABL). Both utilize a chemical oxygen-iodine laser (COIL), with ABL taking the open cycle approach while ATL the closed cycle. Special Operations Command (SOCOM) is the sponsor of ATL (see Figure 1), which is mounted in the belly of a C-130 aircraft and intended to engage moving targets at approximately ten kilometers. Since ATL is to be utilized in a tactical environment, there is a need for a closed-cycle COIL system, which captures waste chemicals and thus reduces chance of detection by the enemy. As of October 2009, ATL has successfully engaged a moving target, though only produced limited damage [2].

Figure 1.　　　　Advanced tactical laser [From 2]

For strategic applications, the Missile Defense Agency (MDA) is developing ABL, Figure 2. This system is the largest and most complex to attempted as of yet. ABL will utilize a megawatt class COIL integrated on a Boeing 747-400F. Operationally, ABL is intended to operate above 40,000 ft against theater ballistic missiles (TBM), which will be engaged during the boost phase [1]. In addition to its megawatt class COIL, ABL also has two kilowatt-class solid state lasers for target tracking/illumination and atmospheric measurements. A large telescope within the nose mounted turret is used by the beam and fire control systems to focus COIL beam onto a pressurized section of the target. To date, ABL has successfully acquired and tracked a boost missile demonstrating an in flight targeting sequence. Additionally, ABL successfully test fired the COIL on August 18, 2009 using an onboard calorimeter that measured beam characteristics. MDA hopes to successfully engage and destroy a target missile by the end of 2009 [3].

Figure 2.　　　　Airborne laser [From 3]

4

No matter the application, strategic or tactical; airborne, ground based or sea based, all HEL systems require extensive beam control. This is due primarily to the presence of self induced platform jitter and atmospheric disturbances. Integral to proper beam control is the use of adaptive control methods. Additionally, beam control systems require a stabilized line of sight (LOS), which can be supplied by an inertial reference unit (IRU). Adaptive filter and IRU implementations will be discussed in more detail in Sections B and C of this chapter.

B.   BEAM CONTROL METHODS

An HEL system must compensate for time varying disturbances, which requires the use of adaptive control methods to reduce beam jitter [4]. Like classical time invariant control systems, adaptive control can be applied using feedforward or feedback. For a feedforward system (Figure 3), a coherent reference input is detected prior to the control actuators. Such a reference input does not exist for feedback system; see Figure 4. Both feedforward and feedback systems rely on error measurements taken at the target. In the case of an HEL system, the error sensor is a position sensor (PSD) [5].
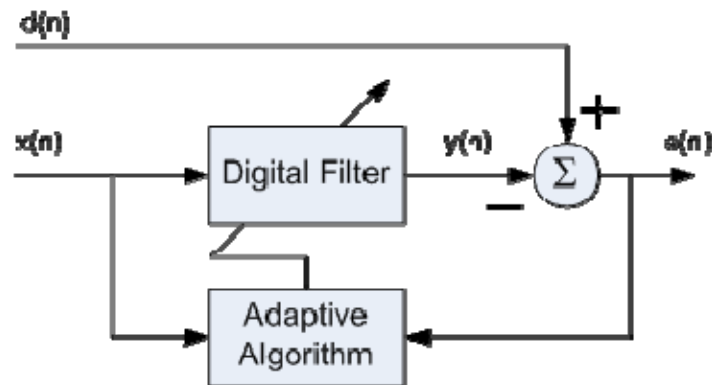
Figure 3.   Feedforward adaptive filter [From 6]
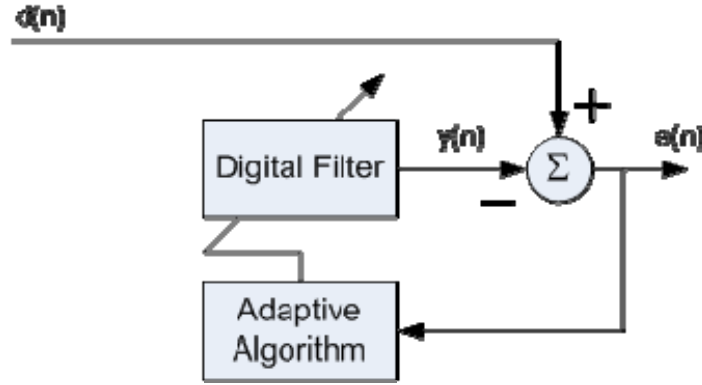
Figure 4.   Feedback adaptive filter [After 6]

In Figures 3 and 4, *d(n)* represents the disturbance, *e(n)* the error as measured at the target, *r(n)* the reference input and *y(n)* the output of the digital filter, which ideally is identical to the disturbance. The digital filter used for the HEL testbed is a finite impulse response (FIR) type filter (Figure 5).
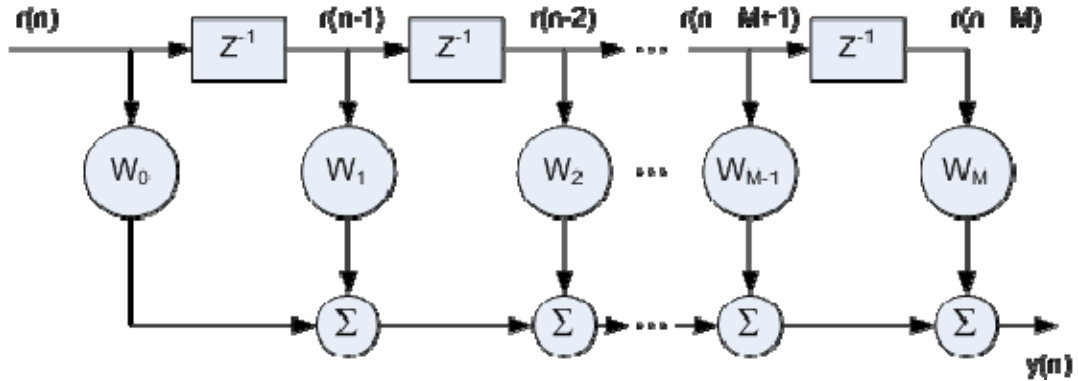
Figure 5.   Structure of digital filter [From 6]

There are two inputs to the FIR filter: a vector of filter weights, *w(n)*, and the reference signal, *r(n),* both consisting of $M+1$ stages. A time delay of one step for each of the $M+1$ stages is used to form the vector of time delayed inputs $\mathbf{r}(\mathbf{n}) = [r(n), r(n-1),..., r(n-M+1), r(n-M)]^T$. Output of the filter is a control signal *y(n),*   which   is   the   inner   product   of   the   weight   vector $\mathbf{w}(\mathbf{n}) = [w_0(n), w_1(n), w_2(n),..., w_M(n)]^T$ and reference signal vector [7]:

6

$$y(n) = \mathbf{w}^T(n)\mathbf{r}(n) \qquad\qquad (1)$$

The error signal *e(n)* is the difference between the disturbance *d(n)* and the controller output *y(n)*, Equation (2). Unfortunately, it is not quite as simple as subtracting *y(n)* from *d(n)*; one must also take into account the dynamics of the actuator itself, since the control signal much pass through a fast steering mirror (FSM) before its effect is sensed at the target. In Equation (2), these secondary plant dynamics are accounted for by the presence of *s(n)*[7].

$$e(n) = d(n) - s(n)y(n) \qquad\qquad (2)$$

A block diagram of Equations (1) and (2) can be seen in Figure 6.
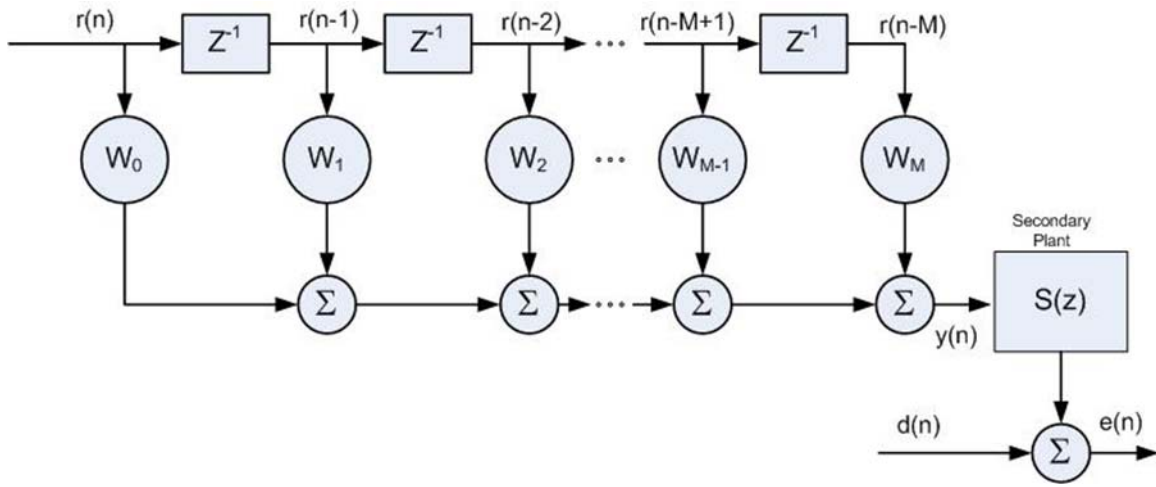
Figure 6.   Block diagram of transversal filter [After 8]

At each time step, the weight vector *w(n)* must be updated, which takes place in the Adaptive Algorithm block of Figures 3 and 4. As with any controller method, the objective is the minimize the target error. An easy way to quantify this is to minimize the mean square of the error signal, $\xi = E[e^2(n)]$ [5]. There are two primary methods of updating minimizing ξ, least-mean-square (LMS) and recursive-least-square (RLS).

1.   Filtered-X Least Mean Squares

Of the two primary methods, least-mean-square (LMS) is simpler and computationally less expensive. LMS uses a gradient approach to determine the steepest descent for minimizing ξ. In [9], it is shown that the weight vector can be computed based on the following:

$$\mathbf{w}(n+1) = \mathbf{w}(n) + \mu\mathbf{r}(n)e(n) \tag{3}$$

Steps of size μ are taken as the filter converges to an optimal weighting vector. A small step size generally results in slower convergence to a value closer to optimum, where as a larger step size may produce oscillations about the optimum weightings.

As stated earlier, controller output pass through the secondary plant (in our case an FSM), prior to its effects being measured at the target sensor. If unaccounted for, phase and gain variation will occur between the error and reference signals. By placing a copy of the secondary plant transfer function, $\hat{S}(z)$, in the reference signal path to the weight updating algorithm of Equation (3), such variations can be avoided [7].

$$\hat{\mathbf{r}}(n) = \hat{s}(n)*\mathbf{r}(n) \tag{4}$$

This is Filter-X method (FX-LMS), which prevents an unstable controller. In simple terms, the reference signal, $r(n)$, is filtered prior to the weight updating algorithm rather than prior to the transversal filter [7].

2.   Filtered-X Recursive Least Mean Squares

Another method of updating the weighting vector is the use of recursive-lease-squares (RLS), which provides faster convergence and lower steady state errors than LMS. The same FIR filter is utilized for RLS as LMS, the difference being the algorithm used for weight updating. The RLS algorithm contains a cost function, which maintains a memory of errors according to a forgetting factor of $0 < \lambda \leq 1$ (there is no such cost function (ξ) memory for LMS, which only uses the current error).

Where LMS attempts to minimize the mean square of the current error, the RLS algorithm minimizes a summation of the square of all errors multiplied by the forgetting factor, λ [7]:

$$\mathcal{E}(n) = \sum_{i=1}^{n} \lambda^{n-i} e^2(i) \qquad (5)$$

The purpose of the forgetting factor is to more heavily weight recent data so that nonstationary disturbances can be accounted for. Development of the RLS computations requires a significant amount of linear algebra, which is explained detail by Kuo [7] and Haykin [9]. Equations (6), (7), and (8) summarize the FX-RLS algorithm for updating the weighting vector $\mathbf{w}(n)$ at each time step.

$$\mathbf{k}(n) = \frac{\lambda^{-1}\mathbf{Q}(n-1)\hat{\mathbf{r}}(n)}{1 + \lambda^{-1}\hat{\mathbf{r}}^T(n)\mathbf{Q}(n-1)\hat{\mathbf{r}}(n)} \qquad (6)$$

$$\mathbf{w}(n) = \mathbf{w}(n-1) + \mathbf{k}^T(n)e(n) \qquad (7)$$

$$\mathbf{Q}(n) = \lambda^{-1}\mathbf{Q}(n-1) - \lambda^{-1}\mathbf{k}(n)\hat{\mathbf{r}}^T(n)\mathbf{Q}(n-1) \qquad (8)$$

As with the FX-LMS algorithm, the reference signal is filtered through the secondary plant dynamics, as indicated by $\hat{\mathbf{r}}$. Another advantage of the RLS methods is that the weighting values will approach those of the optimal Wiener filter weightings, which is not the case for LMS [7].

3. Reference Signal

The FX-LMS and FX-RLS algorithms have been applied using a single-channel reference signal in the research of [10],[11], and [12]. Additionally, in [8], two methods of incorporating multiple reference signals are implemented. In that case, the reference signals consisted of an accelerometer and PSD. In this thesis, multiple reference signals are also utilized, those being a gyro signal and again a PSD.

C. INERTIAL REFERENCE UNITS

The HEL testbed at NPS contains an imaging sensor with a frame update rate of 200 Hz for the narrow field of view (NFOV). Due to the limited frame rate, the system is unable to effectively reject high frequency jitter. Additionally, the even if it had a high

frame update rate, the NFOV imaging sensor would be unable to detect rigid mode vibration. For these primary reasons, an inertially stabilized line of site (LSO) is required. In order to achieve a stabilized LOS, some type of inertial reference unit (IRU) is needed. Such a unit will control high bandwidth FSMs, which cancel the effects of optical jitter. There are two primary IRU approaches; stabilized inertial sensors and strapdown inertial sensors. Both stabilization methods inject a reference beam into the telescope, which follows the same optical path as incoming imagery as well as the outgoing high energy laser [13]. Research to date on the HEL testbed has been with a strapdown version of the IRU.

1. Stabilized Inertial Sensor

A stabilized inertial sensor system is one in which a stabilized reference laser is mounted to a gimbaled platform. See Figure 7 for a simple block diagram of a stabilized IRU. A closed loop control system is used to drive actuators on the platform, thus creating an inertially stabilized output. The reference laser, also attached to the gimbaled platform, is then able to supply an inertially stabilized reference beam. Since this beam is injected into the same optical path as both incoming imagery and outgoing laser energy, one is able to determine optical path jitter. An FSM can then be used to cancel the effects of such jitter. Additionally, track sensors are used to command the platform inertial sensors and therefore compensate for target motion. A major advantage of a stabilized inertial system is that an exact transfer function representing dynamics between the reference laser and the corrective element is not required [13].
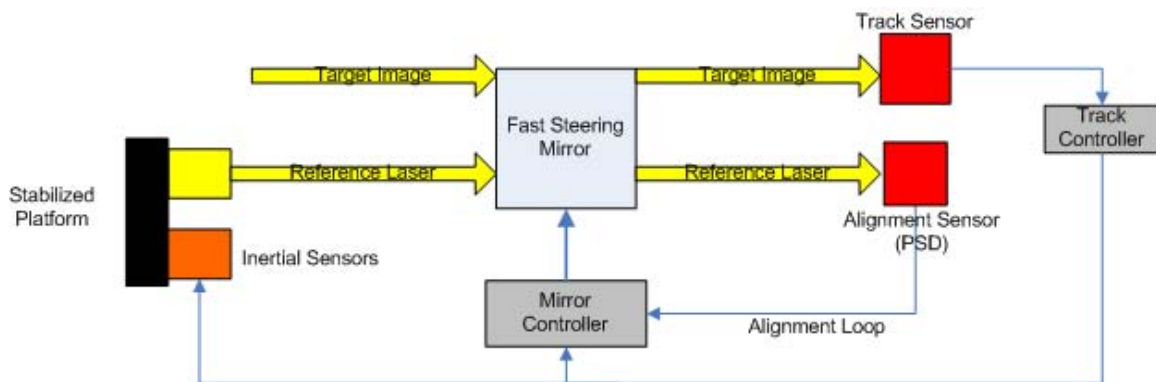
Figure 7.   Block diagram of stabilized IRU

10

2. Strapdown Inertial Sensor

The strapdown inertial sensor setup is the simpler of the two methods. In this system, inertial sensors are rigidly mounted to the HEL system and measure base motion, see Figure 8 for a simple block diagram of such a system. In addition, the reference laser is rigidly attached to the inertial sensors and thus provides alignment of the optical path to the sensor frame. A feedforward signal from the strapdown sensors is used to command an FSM, which cancels the effects of jitter on the optical path. As with the stabilized system, track sensor measurements are used to compensate for target motion. While strapdown systems are simpler and cheaper to build, they are prone to error caused by inaccurate transfer function knowledge [13].
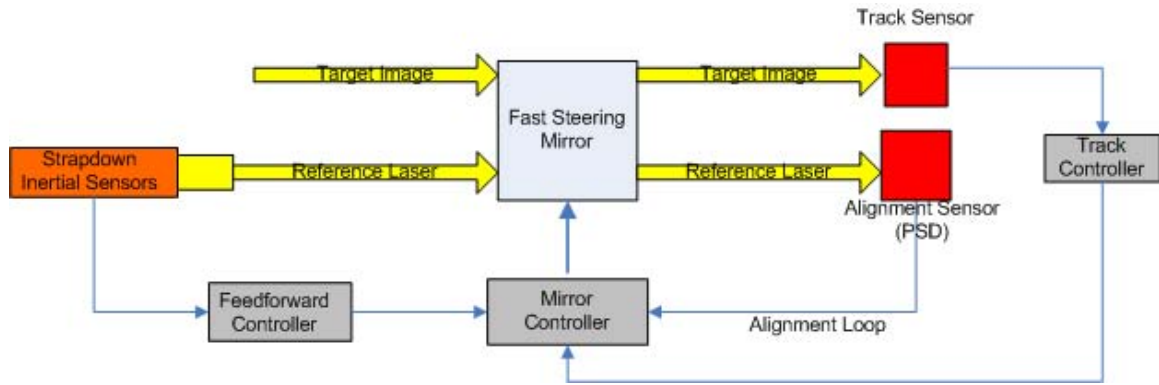
Figure 8.   Block diagram of strapdown IRU

THIS PAGE INTENTIONALLY LEFT BLANK

III.   NPS HEL TESTBED

The objective of the HEL testbed is to provide a research environment for development of new technologies related to target acquisition, pointing, tracking and jitter control (see Figure 9). In this chapter, a brief overview of the testbed is provided. For more detailed information about the NPS HEL testbed, refer to [6], which is an in depth report on its characteristics.
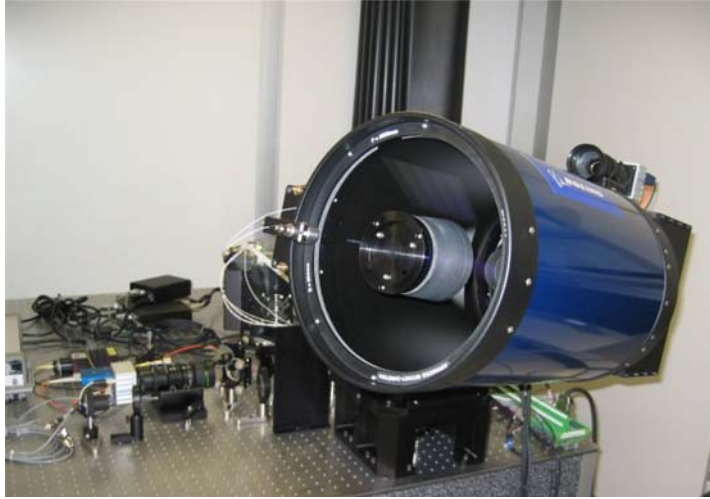
Figure 9.   HEL testbed

A.   SYSTEM CONFIGURATION

HEL testbed is composed of three major components; host computer, target computer, and beam control system (Figure 10). The host computer manages system operation modes and all sub-systems through user interfaces. Real-time code is executed on the target computer, which directly controls the beam control system. This system is composed of three feedback loops: two position control loops and one rate control loop, as shown in Figure 11. In addition to these three major components, a moving target with an illuminated light source and corresponding position sensing device (PSD) provides evaluation of system performance.
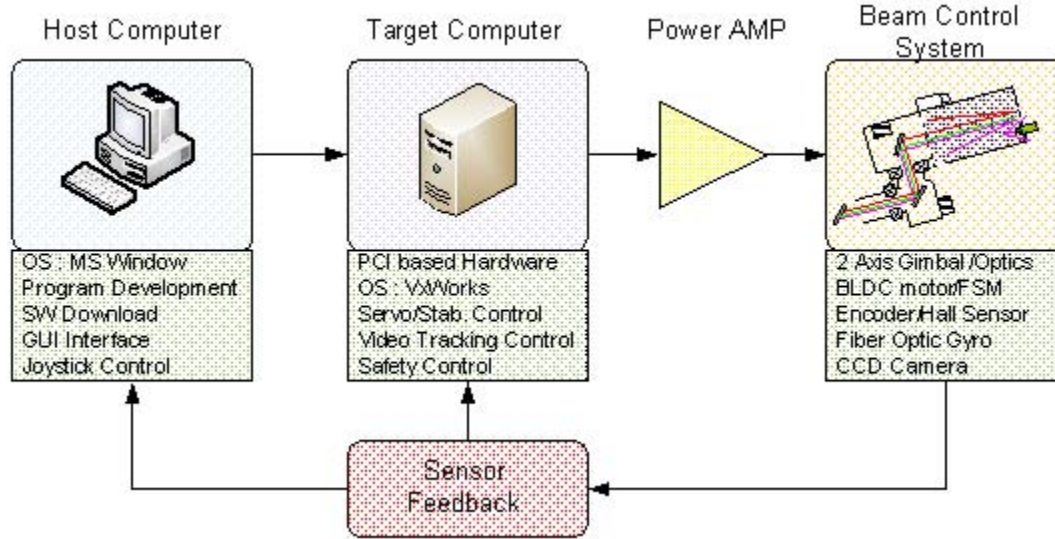
Figure 10.   HEL system configuration
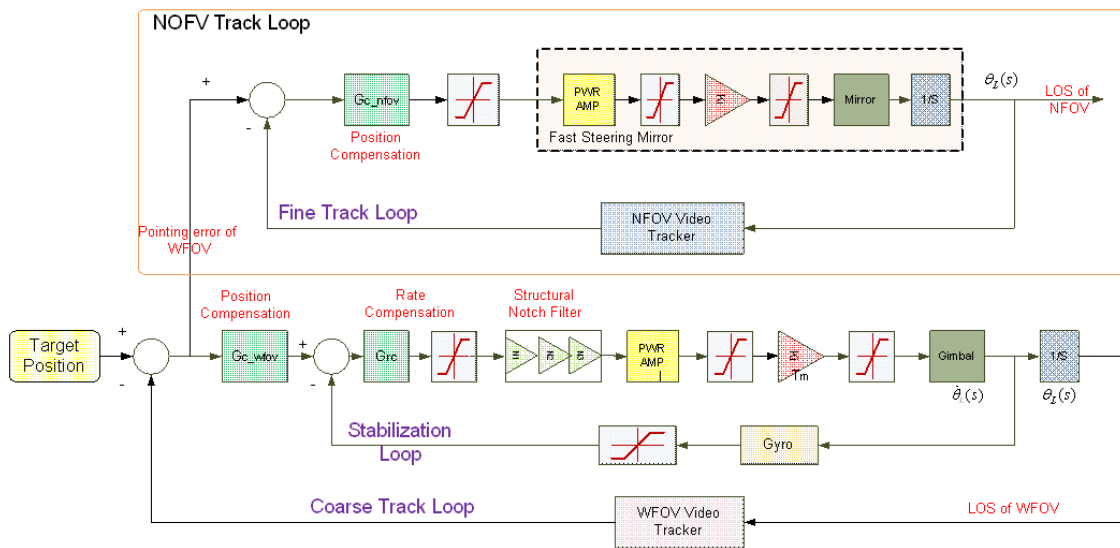
Figure 11.   Control block diagram

1.   Host Computer

An MS Windows-based personal computer, on which all software is developed, compiled and debugged, acts as the host computer. An Ethernet connection is used to download final object code to the target computer. The host computer also provides a means for user input. Motion commands are generated by a two-axis joystick, which also includes system operation control switches. Additionally, menu driven interfaces are also

implemented to control the wide field of view (WFOV) and narrow field of view (NFOV) video parameters. Modes include video mode, track mode, gate size, and video tracking algorithm.   Figure 12 is an example of the WFOV user interface, a similar one is provided for the NFOV.
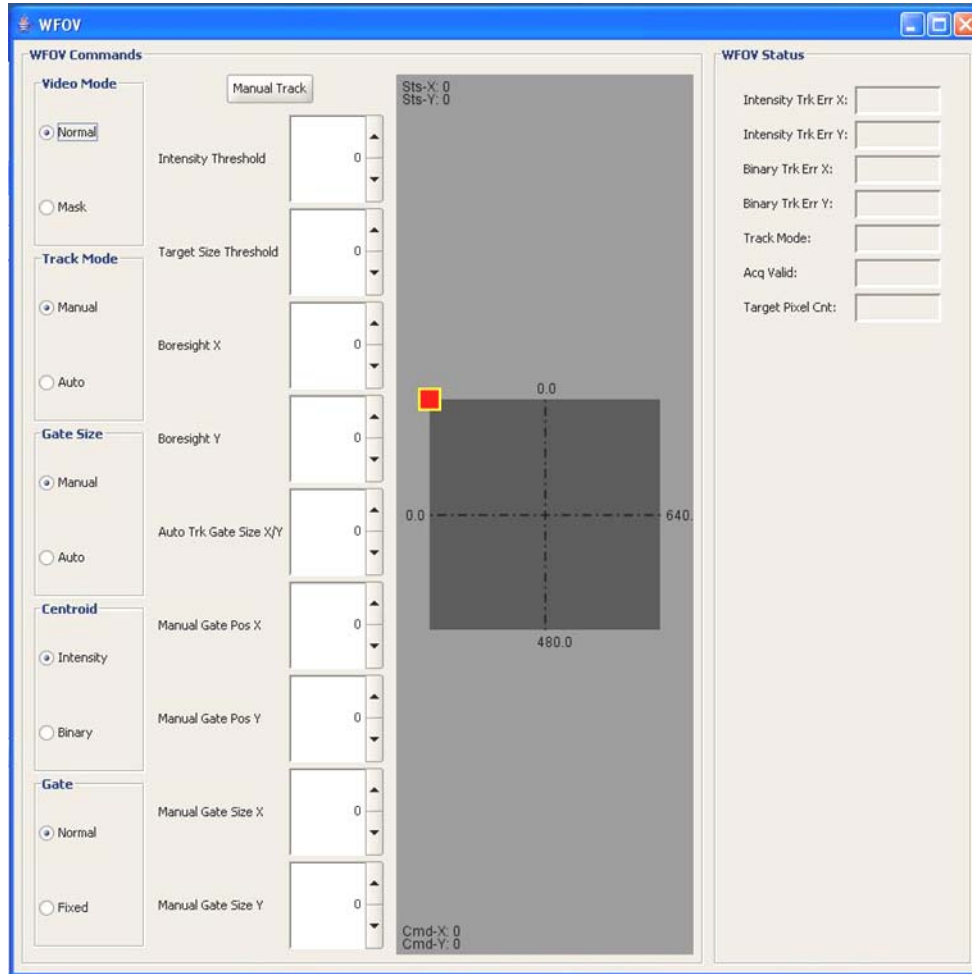
Figure 12.   WFOV user interface

2.   Target Computer

The target computer is a Vxworks-supported CompactPCI-based system consisting of four 3U size boards: PowerPC CompactPCI processor board (IMP2A), IO Pack Carrier Board (ACP8630), Multifunction CompactPCI Board (ACPC730), and Counter Timer Board (ACP484). Real-time code is executed by the PowerPC board, which also controls all subsystems. A frame grabber PMC card is also mounted on the

15

board to control and communicate with the WFOV and NFOV cameras, which are connected by camera link. This board also communicates with the host computer via Ethernet, from which it downloads software code and receives control commands. Angular rate data is received from the gyros by a synchronous interface, which is connected to a PMC module on the IO Pack carrier board. Monitoring of analog input signals is accomplished with the multifunction board. See Figure 13 for an external interface diagram; the characteristics of the four boards in the target computer are summarized in Table 1.

Figure 13.   External interfaces of target computer

Table 1.   Target computer characteristics

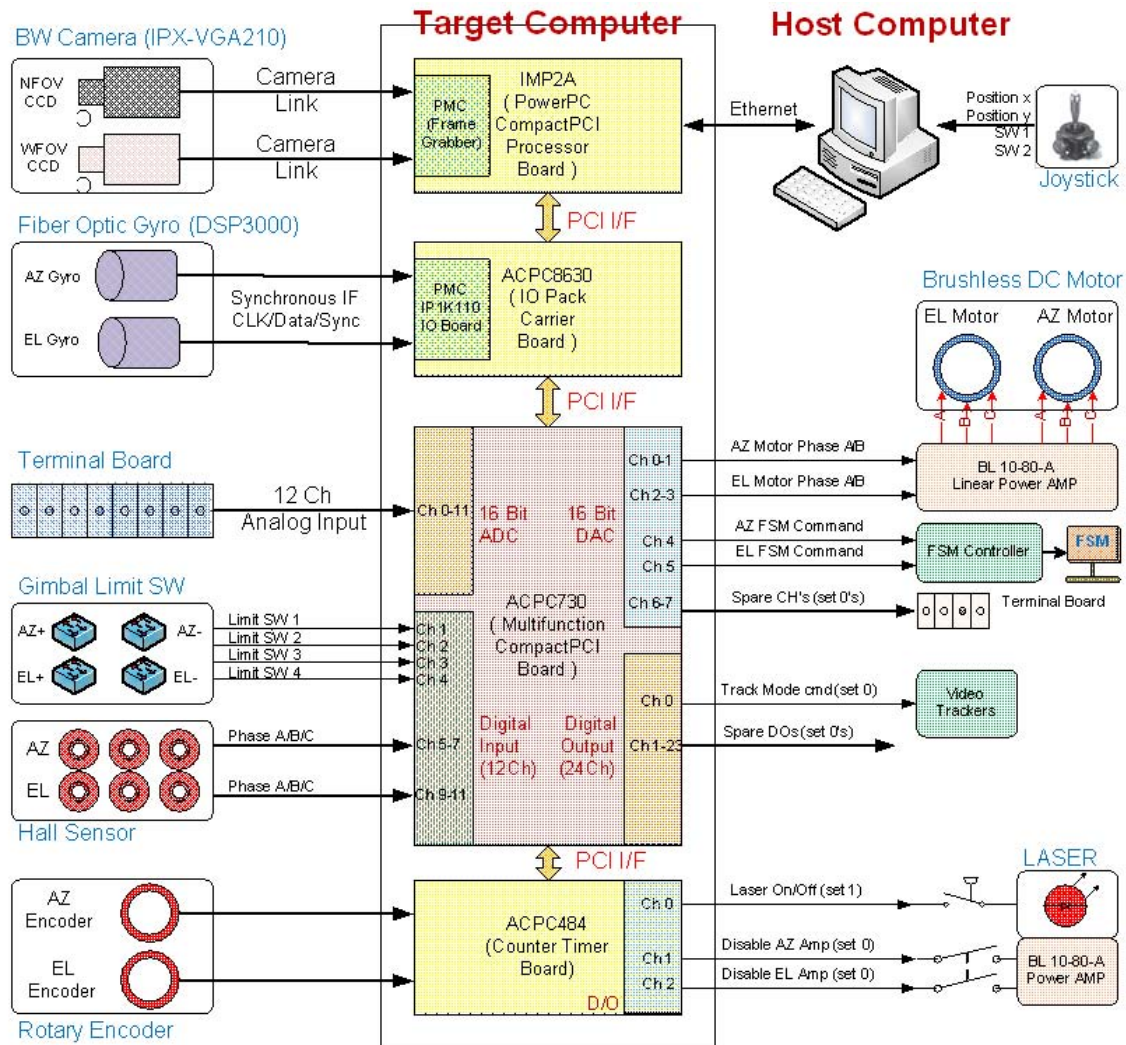| Board type	Model	Characteristic
PowerPC board	IMP2A	• 1.4GHz PowerPC 7448, 3U CompactPCI SBC • 256 Mb SDRAM, 1Mb on-chip cache, 128Mb flash • 2 Ethernet, 2 serial ports, 4 bits GPIO • PCI-x capable PMC slot
IO Pack Carrier board	ACPC8630	• Carrier for Industrial I/O Pack Mezzanine board
Multifunction board	ACPC730	• 16 bit ADC : 16 differential or 32 single ended, 100KHz conversion rate (10uS conversion time) • 16 bit DAC : differential type, 80.8KHz conversion rate (12.375uS conversion time) • 32 bit Counter/Timer : waveform generation, event counting, watchdog timing, pulse width and period measurement • 16 Digital Input/Output channels
Counter Timer board	ACPC484	• Six 32 bit multifunction counter/timer : position measurement, pulse width modulation, watchdog timer, event counter, frequency measurement • 16 digital input/output channels

3.   Beam Control System

Components of the beam control system include WFOV and NFOV track loops, alignment and interface optics, reference laser and surrogate HEL. A schematic of the beam control system is shown in Figure 14, while a breakdown list is shown in Figure 15. To create an optical path from/to the laser source, target and sensors, a number of mirrors, lenses, and beam splitters are mounted on the optical table. When originally constructed, the HEL testbed also included an analog auto alignment control loop, which continuously detected and corrected misalignment between the reference laser and a position sensing devise (PSD) [6]. As part of the thesis, this analog loop was replaced by a digital controller using adaptive control methods. The new auto alignment control loop will be discussed in more detail in Chapter IV.

17
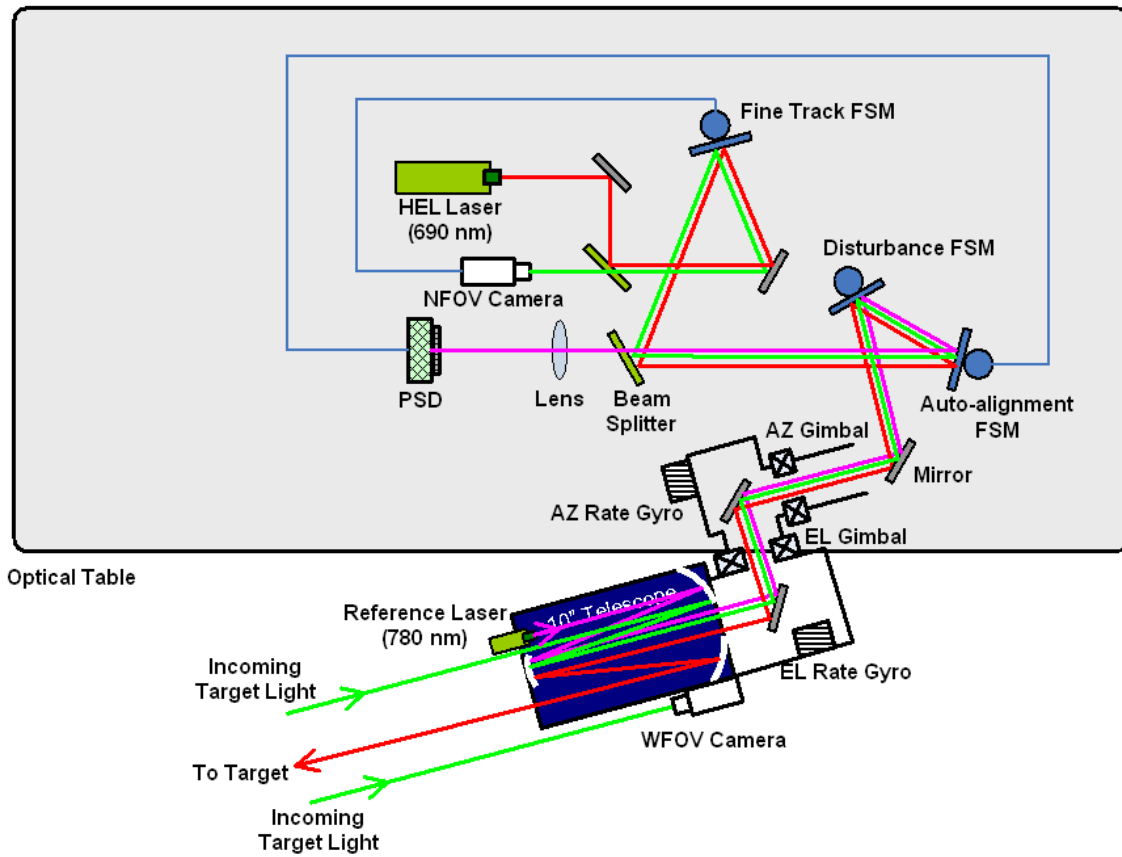
Figure 14.   Schematic of beam control system

18
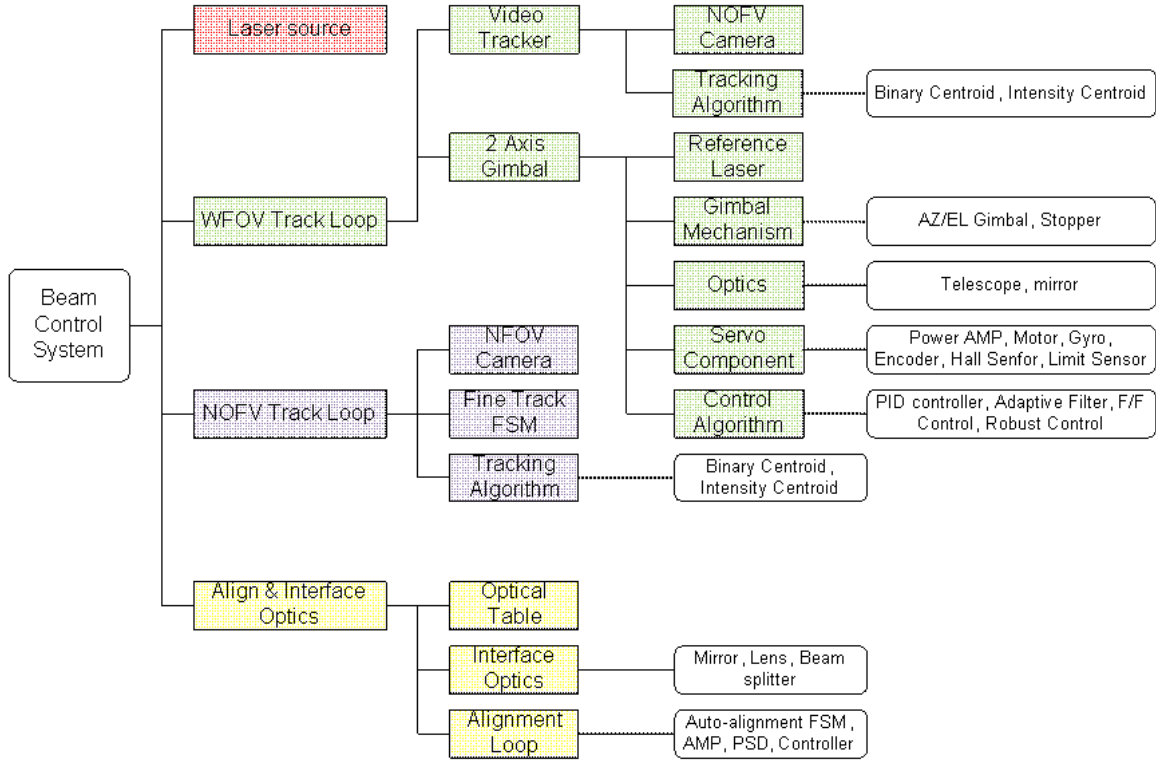
Figure 15.   Breakdown list of beam control system

a.   WFOV Track Loop

Two feedback control loops, inner and outer loop, comprise the WFOV track loop as seen in Figure 16. The inner loop is a rate control loop composed of a gimbal, power amplifier, controller, and servo components (gyro, motor, and encoder). Primary purposes of the inner loop are to maintain LOS to a target in inertial space with respect to external disturbance, and track input rate commands from the WFOV tracker. The WFOV camera and a video tracking algorithm comprise the outer loop, which is a position control loop. This loop calculates the error between LOS and target center, sending an error signal to the rate command of the inner control loop [6].
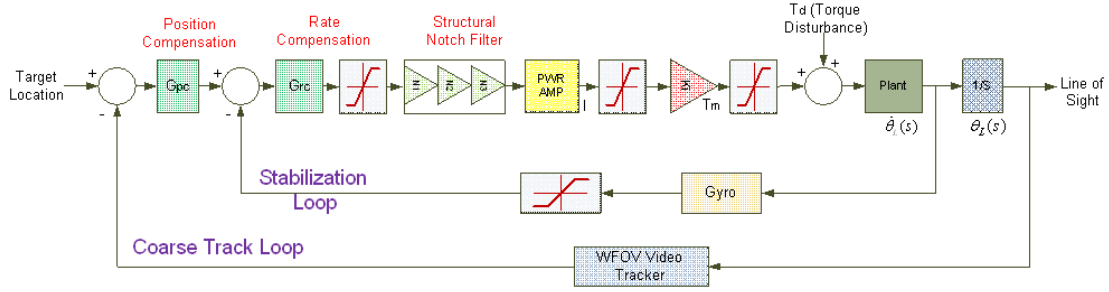
Figure 16.   WFOV track loop

b.   *NFOV Track Loop*

The NFOV track loop is a position control loop. It is composed of the NFOV camera, fast steering mirror (FSM), and a video tracking algorithm, see Figure 17. As with the WFOV track loop, the NFOV track loop calculates error between the LOS and target. In this case, though, the errors are much smaller than can be compensated for by the WFOV, thus minimizing pointing error between the target and LOS.
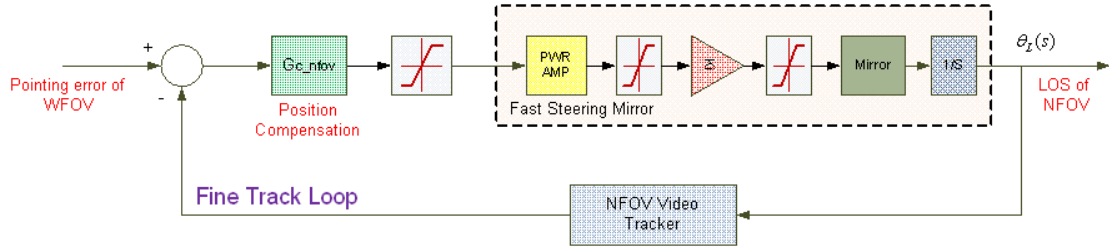
Figure 17.   NFOV track loop

B.   SYSTEM CHARACTERIZATION

A number of experiments were performed to determine characteristics of the HEL testbed with the results used for system modeling. Experiments included resonant frequency test, rate loop servo bandwidth and stabilization test, FSM test, and NFOV bandwidth test. See Figure 18 for test configuration. An external terminal board on the target computer provided an interface for signals between the beam control system and target computer, in addition to providing input/output test points. Test signal generation, data storage and observation of signals were conducted using a dynamic signal analyzer, data acquisition system, and oscilloscope.

20
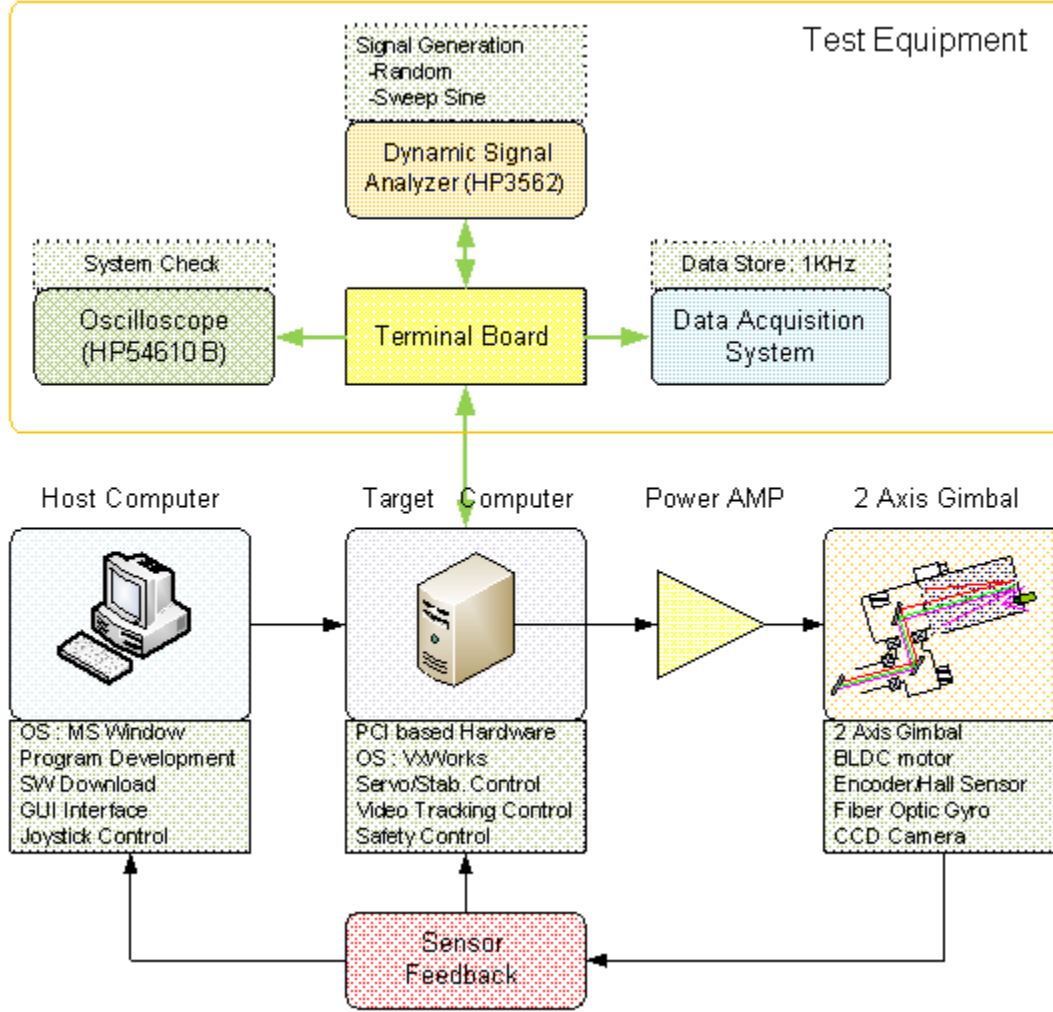
Figure 18.　　Configuration for system characterization experiments

1.　WFOV Control Loop

a.　*Resonance Frequency*

　　　Random signals were applied to the power amplifier and output signals were received at the gyro and encoder, respectively. Test input and output points are shown in Figure 19. Data analysis flow for resonance frequency determination is shown in Figure 20. Resonance frequencies were calculated using power spectral density analysis. Prior to performing the analysis, preprocessing was required to remove constant drift in addition to outliers. A periodogram for a data sequence, $[x_1, x_2, \cdots, x_n]$, was chosen for power spectral density computation as given by Equation (9). To suppress

spectral noise, an average of 20 power spectral density computations was conducted. Resonance testing was performed over a frequency range of 0–200 Hz with an input magnitude of 1–2V, as summarized in Table 2.
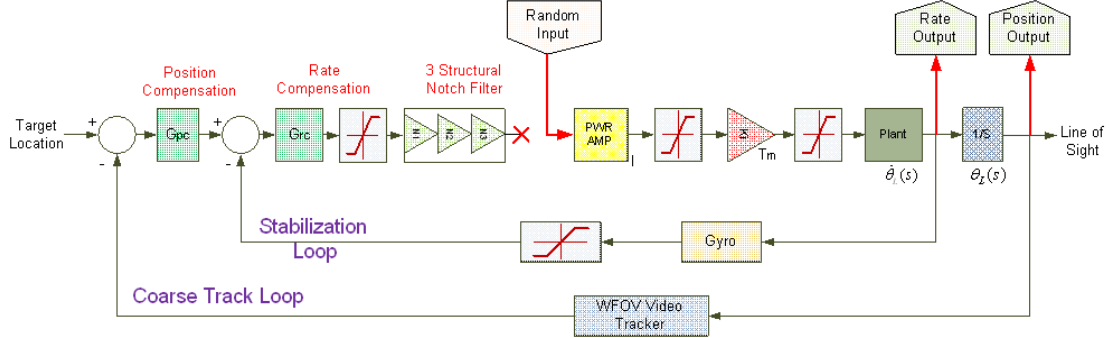
Figure 19.　　　Resonance frequency test points
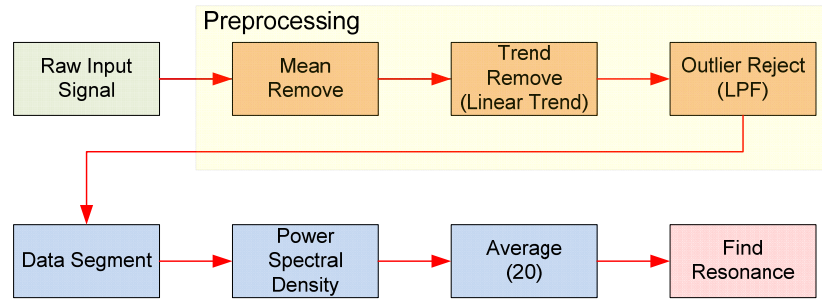
Figure 20.　　　Analysis flow for resonance determination

$$S(e^{jw}) = \frac{1}{n} | \sum_{k=1}^{n} x_k e^{-jwk} |^2 \qquad (9)$$

Table 2.　　WFOV resonance testing scenarios

Dir.	Input (Vpeak)	Output Data	Time Length (sec)	Measured Data Analysis	
				Freq. Range (Hz)	Average No.
EL	1.0	Gyro	8	0-100	20
	1.0	Gyro	4	0-200	20
	1.0	Encoder	8	0-100	20
	1.0	Encoder	4	0-200	20
AZ	1.0	Gyro	8	0-100	20
	1.0	Gyro	4	0-200	20
	2.0	Encoder	8	0-100	20
	2.0	Encoder	4	0-200	20

Over the wide frequency range used in testing, a number of resonance frequencies were measured, as summarized by Table 3. The lowest resonance frequency of the elevation axis is higher than that of the azimuth axis, since the elevation axis gimbal mechanism is smaller, more rigid and simpler. Additionally, the gyroscopes contain many more resonance frequencies than the encoders since they detect angular velocity versus only angular position for the encoder.

Table 3.   Summary of WFOV resonance frequency testing

Direction	Output signal	Resonance frequencies (Hz)
AZ	Gyro	2.6, 8.3, 11.4, 15.9, 36.6, 69.5, 101, 134, 147.7
	Encoder	2.6, 8.2, 11.4, 101
EL	Gyro	3.8, 10, 14.9, 43.3, 61.4, 74.5, 101, 145, 195
	Encoder	3.8, 11.6, 61.4, 101

b.   *Rate Loop Servo Bandwidth*

Rate loop bandwidth was measured by applying a sweep sine signal to rate command and observing output at the gyro. Test scheme is shown in Figure 21, and data analysis flow in Figure 22. As with resonance testing, preprocessing was conducted for trend removal and outlier rejection. Input voltage was 0.02V for elevation axis, and 0.05V for azimuth axis. Data was measured from 1–50Hz for both axes.
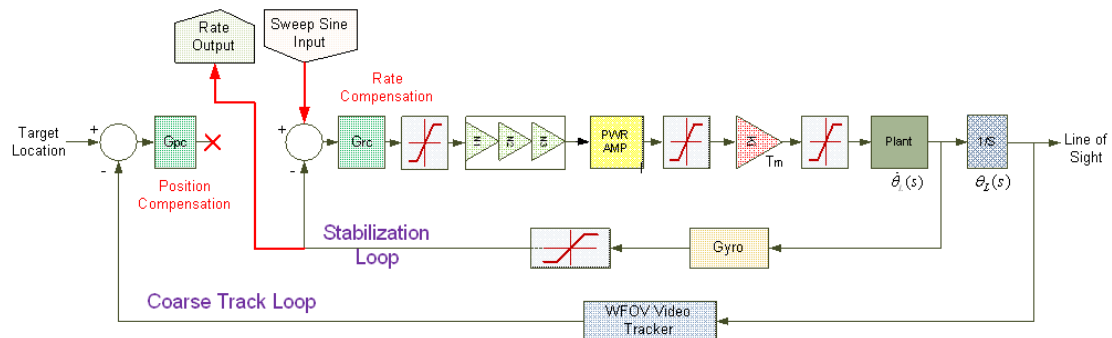

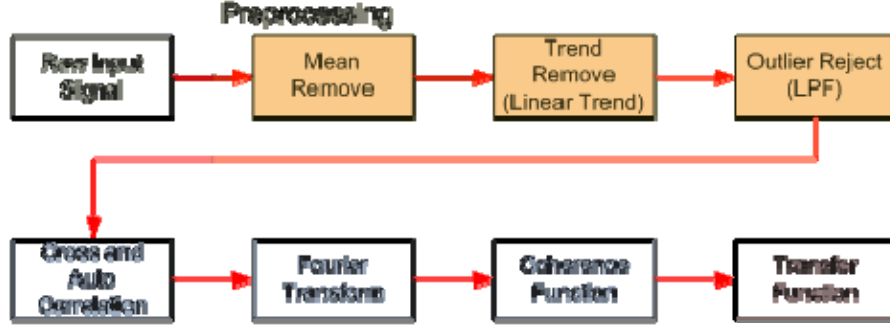Figure 21.   Rate loop servo bandwidth test schematic

Figure 22.   Rate loop servo bandwidth data analysis flow

The ultimate goal of this testing was to determine the transfer function of the rate loop servos. Several intermediate calculations were required to make this determination, the first of which is the cross-correlation sequence as given by

$$R_{xy}(m) = E[x_{n+m} \cdot y_n^*] = E[x_n \cdot y_{n-m}^*] \tag{10}$$

where x_n and y_n are jointly stationary random processes, and $E[\bullet]$ is the expected value operator. In reality, a correlation estimate given by Equation (11) had to be used since only a finite segment of one realization of the infinite length random process was available.

$$\hat{R}_{xy}(m) = \begin{cases} \sum_{n=0}^{N-m-1} x_{n+m} \cdot y_n^* & m \ge 0 \\ \hat{R}_{yx}^*(-m) & m < 0 \end{cases} \tag{11}$$

Additionally, coherence function calculation was also required. Coherence shows the portion of the output spectrum related to the input spectrum as given by Equations (12)-(14)

$$\gamma^2 = \frac{G_{xy} \cdot G_{xy}^*}{G_{xx} \cdot G_{yy}} \tag{12}$$

$$G_{xy} = FFT(\hat{R}_{xy}) \tag{13}$$

$$G_{xx} = FFT(\hat{R}_{xx}) \tag{14}$$

where G_{xy} is the cross spectrum and G_{xy}^* is its complex conjugate, G_{xx} is the input power spectrum and G_{yy} the output power spectrum.

24

Coherence is an indication of statistical validity of frequency response measurements, and is measured on a scale of 0.0–1.0, with a value of 1.0 corresponding to perfect coherence. Reasons for a coherence value less than one include poor resolution, nonlinearities, extraneous noise and uncorrelated input signals. Additionally, it is independent of the shape of the frequency response function since it has been normalized. Finally, the frequency response, also called the "Transfer function," is calculated based on a ratio of the cross spectrum to input power spectrum as given by

$$H(f) = \frac{G_{xy}}{G_{xx}} \tag{15}$$

Gyro output for the azimuth axis is shown in Figure 23, while elevation axis gyro output is shown in Figure 24. Significant steady state errors were observed for both axes. Transfer function results are shown in Figures 25 and 26. The 3dB bandwidth is 6Hz for the azimuth axis, and 7Hz for elevation. Additionally, resonance frequencies in the azimuth axis of 8.2Hz, 11.4Hz, and 15.9Hz caused significant reduction in tracking performance.
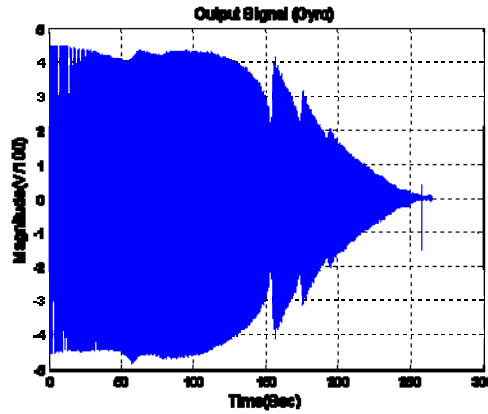

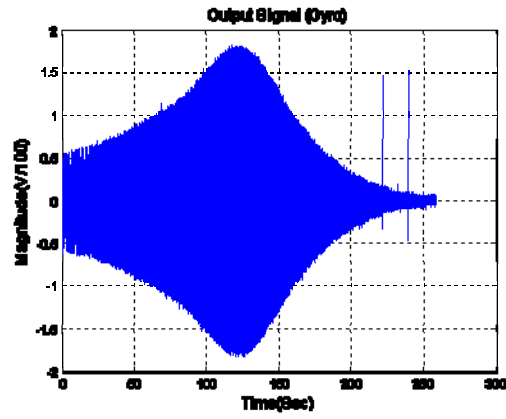Figure 23.   Azimuth axis gyro output

Figure 24.   Elevation axis gyro output
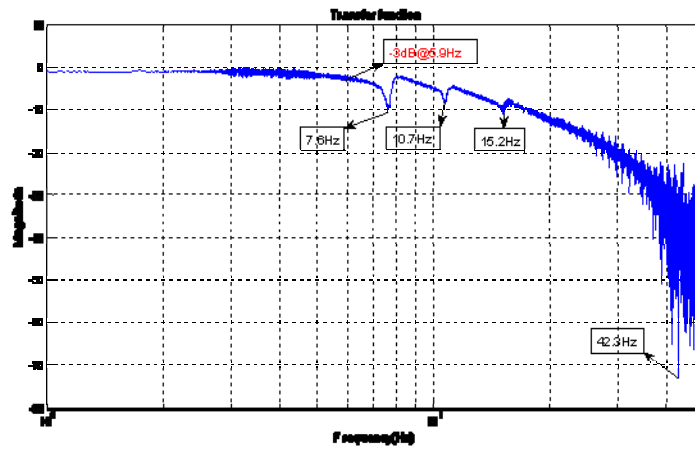
Figure 25.   Azimuth axis transfer function
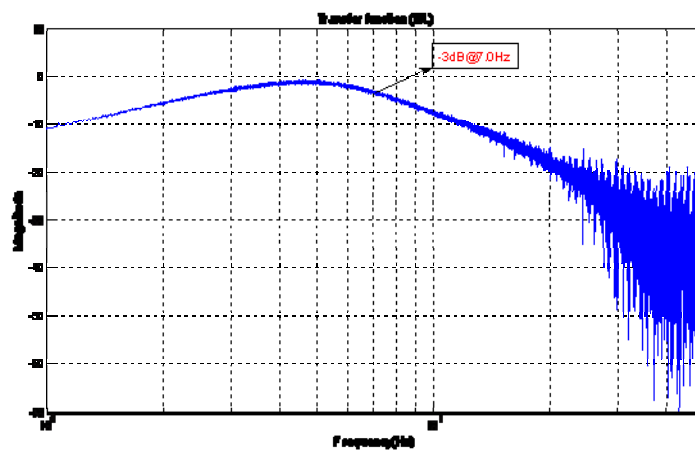
Figure 26.   Elevation axis transfer function

c.   *Rate Loop Stabilization*

By applying a disturbance to the input of the power amplifier and measuring torque error, one is able to determine the torque rejection characteristics. Disturbance input was a 0.5Vpk sweep sine signal over the frequency range of 1–100Hz. Test scheme can be seen in Figure 27.
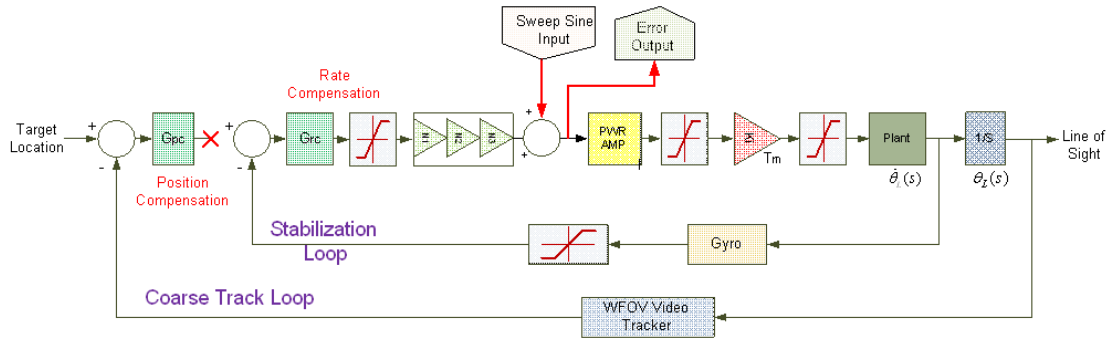
Figure 27.   Rate loop stabilization test scheme

Error output in the time domain is seen in Figures 28 and 29, while frequency domain output is shown in Figures 30 and 31. Test results show the torque rejection ration is low over the tested frequency range. Additionally, stabilization and servo tracking performance were adversely affected by resonance frequencies.
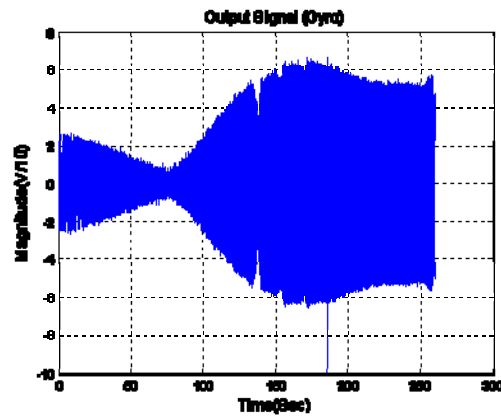
Figure 28.   Azimuth error output
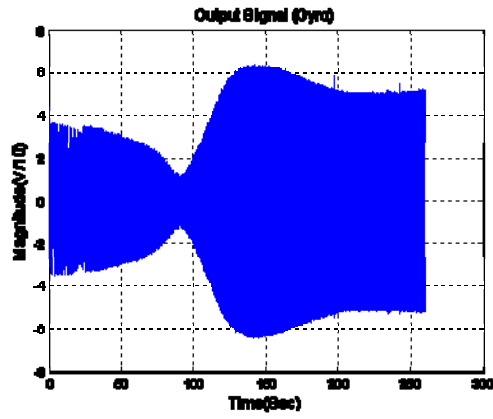
Figure 29.   Elevation error output
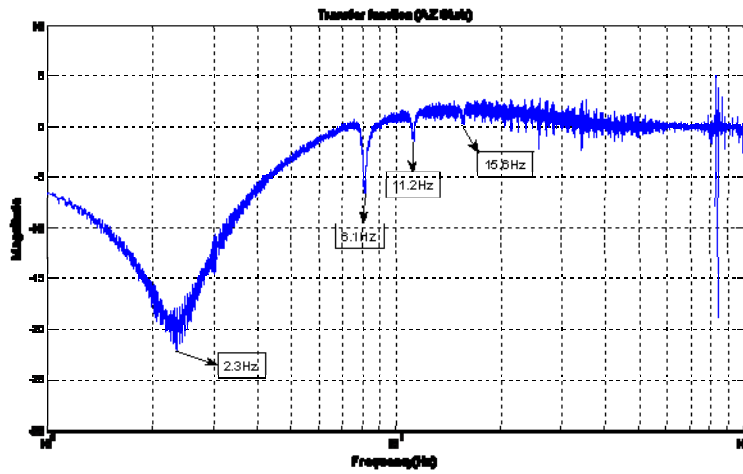
Figure 30.   Azimuth rate stabilization transfer function
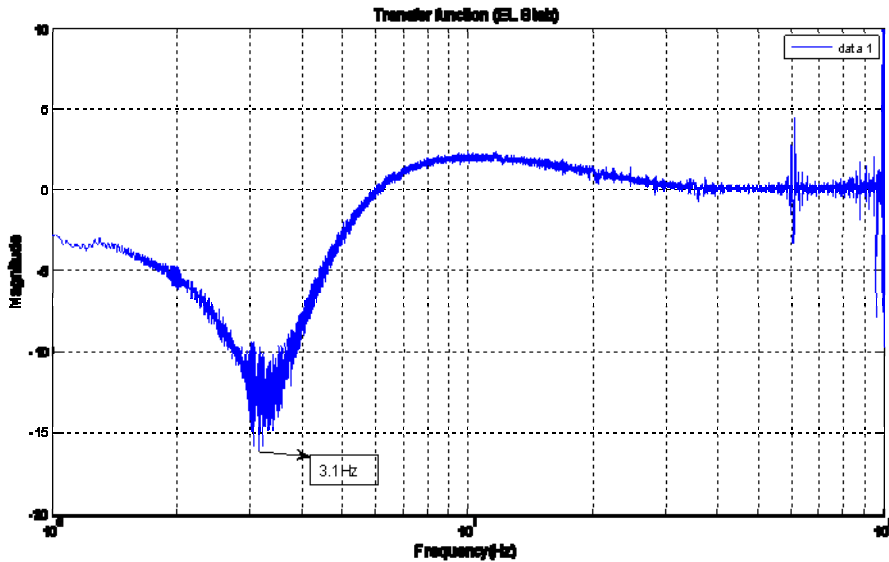
Figure 31.　　　Elevation rate stabilization transfer function

2.　NFOV Control Loop

a.　Fast Steering Mirror

FSMs have been used for a number of years for target acquisition, scanning and beam steering. A push/pull configured voice coil drives a two axis mirror. This setup is similar to a speaker coil, with the difference being the FSM is configured with a moving magnet versus a moving coil as is the case for a speaker. The mirror is flexurally suspended and includes an optical sensor as well as a local feedback system. Local position feedback is the inner loop of the NFOV control loop. FSM dynamic characteristics were determined by applying a sweep sine signal to the local position input command and taking output from the position sensor, see Figure 32. Frequency range for the test was 1–1000Hz with an input voltage of 0.5Vpk. Tests were conducted on both azimuth and elevation axis. Results from frequency response tests are shown in Figures 33 and 34. As one would expect, the transfer function in nearly identical between the two axes, and both have a -3dB bandwidth of 360Hz.
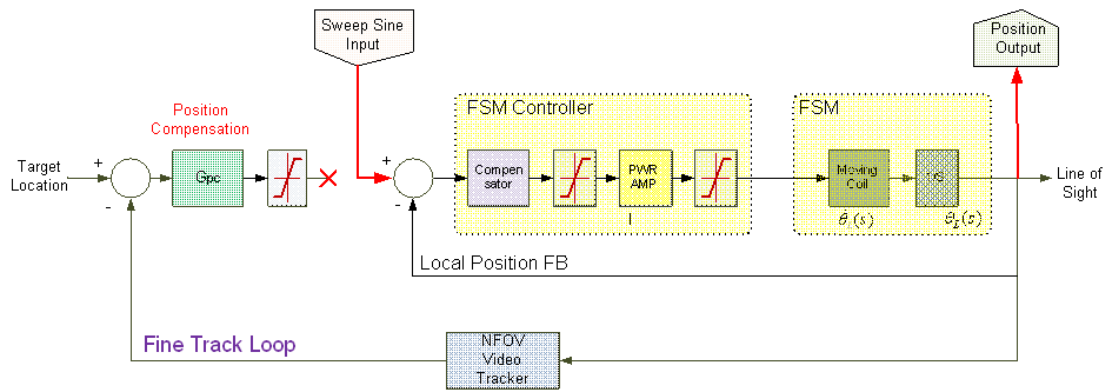
Figure 32.   Test points for FSM testing
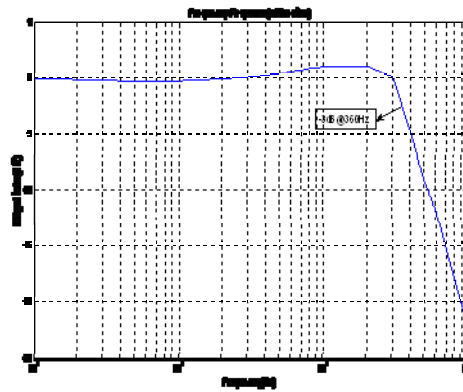
Figure 33.   NFOV azimuth FSM transfer function
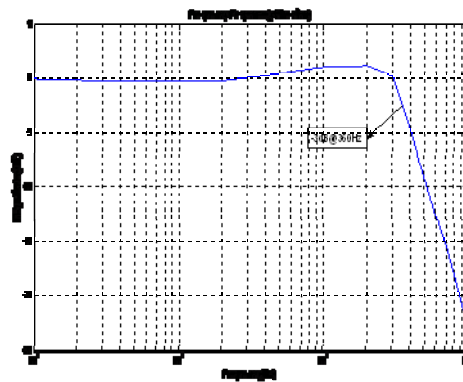
Figure 34.   NFOV elevation FSM transfer function

b.   NFOV Bandwidth

Ideally, one would be able to use a test scheme as shown in Figure 35 to determine the frequency response of the NFOV video tracker. Unfortunately, in reality it

30

is not so simple due to numerous difficulties generating sweep sine target motion, and a lack of target position values. An alternative scheme using two FSMs, as seen in Figure 36, was actually used for bandwidth testing. A sweep sine signal is applied to the position input of the first FSM and the output signal is measured as the position output of the second FSM. Test signals magnitudes were 0.5V and 1.0V over a frequency range of 0.1-100Hz, as summarized in Table 4.
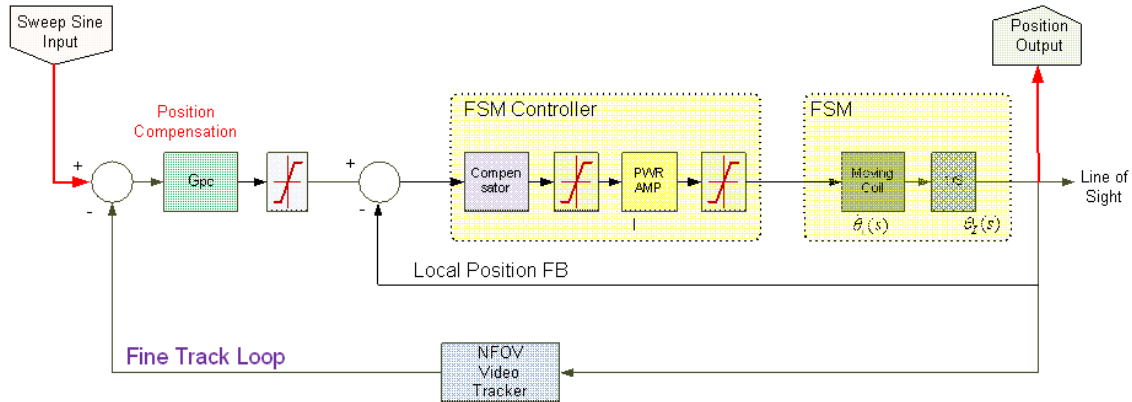
Figure 35.   Ideal test setup for NFOV track loop testing
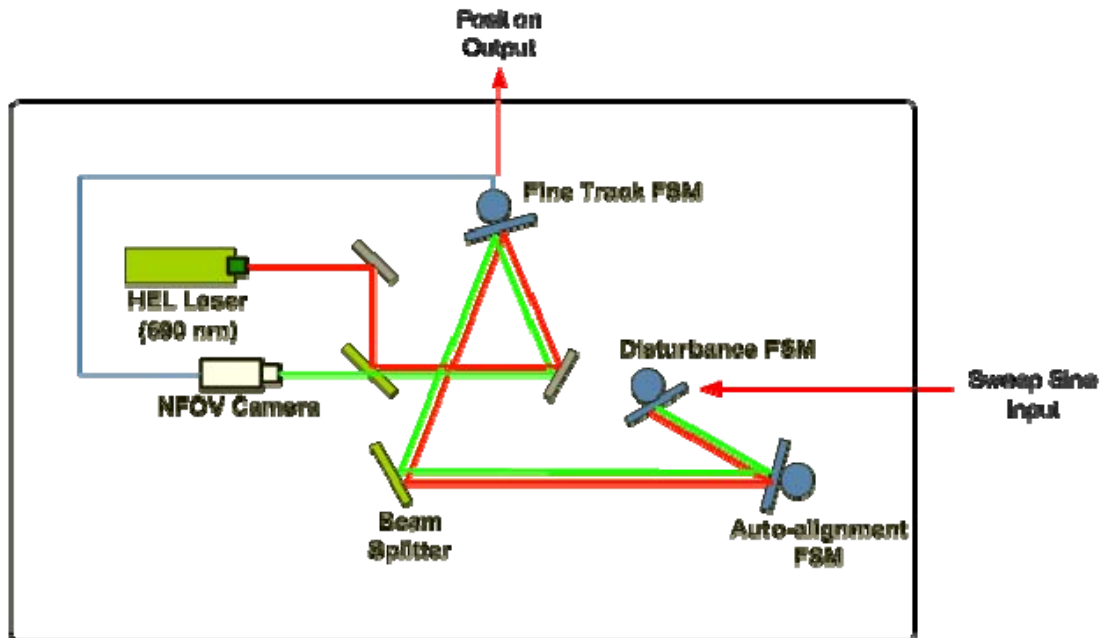
Figure 36.   Actual test setup for NFOV track loop testing

31

Table 4.   Scenario for NFOV track loop test

| No. | Dir. | Input (Sweep sine) | | | Fine Track FSM Output Pin |
		Disturbance FSM Input Pin	Sweep sine Magnitude	Frequency	
1	X	x+ (4)	0.5V(=1.31mil)	0.1~100 Hz	x-Pos (pin 14)
2	(AZ)	x- (3)	1.0V(=2.62mil)	0.1~100 Hz	GND(22,16)
3	Y	y+ (13)	0.5V(=1.31mil)	0.1~100 Hz	y-Pos (23)
4	(EL)	y- (12)	1.0V(=2.62mil)	0.1~100 Hz	GND(22,16)

The transfer function for each axis was nearly identical regardless of input magnitude. In both axes, the -3dB bandwidth was 13Hz, see Figures 37 and 38 for test results.
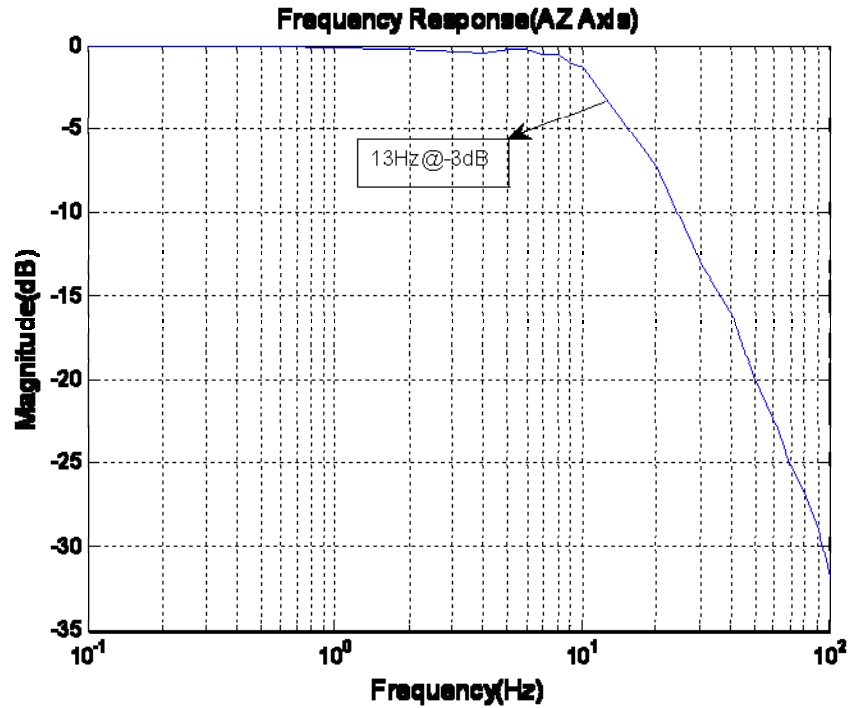
Figure 37.   NFOV video tracker transfer function, azimuth axis
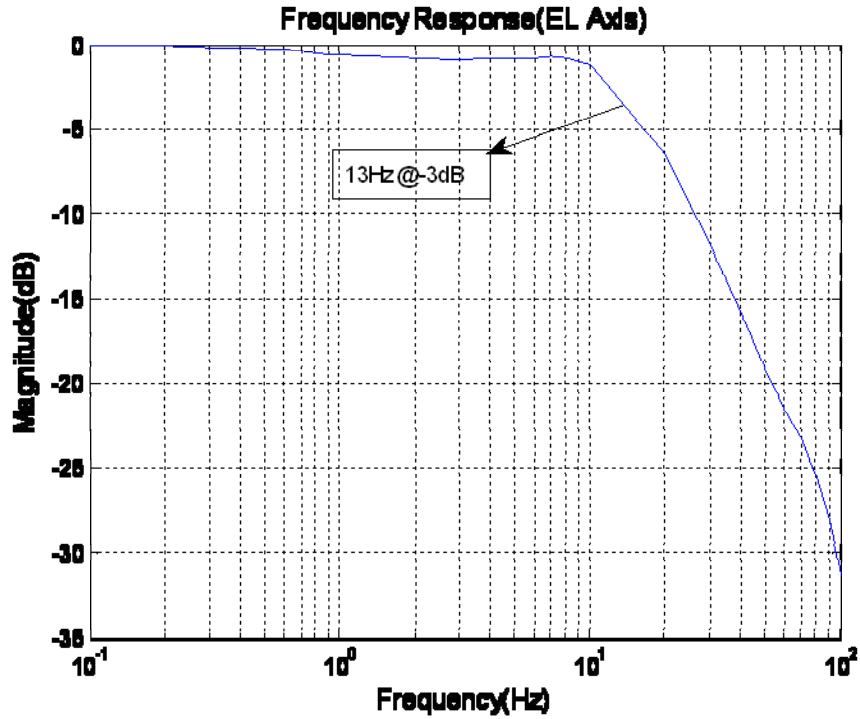
Figure 38.   NFOV video tracker transfer function, elevation axis

C.   MATHEMATICAL MODEL AND SIMULATION

A mathematical model is a good tool for estimating system performance and evaluating the performance improvements associated with new control algorithms. Two methods were used to determine mathematical models for the various HEL testbed subsystems; experimentation and component specification. Specifically, data sheets were the basis for models of the servo components to include gyros and power amplifiers. Based on the component models and experimental results, local control loop and whole integrated models were built using Matlab Simulink.

1.   Component Modeling

The KVH Industries model DSP-3000 (now referred to as the DSP-3400 by KVH industries) gyros are used to measure angular rate of rotation, which is then integrated for accurate angle measurements. The DSP-3000 is a single-axis fiber optic gyro outputting a digital signal over a synchronous serial interface at the rate of 1000/sec. Bandwidth is

an important parameter for dynamic control systems. Since the -3dB bandwidth is greater than 400Hz, the mathematical model of Equation 16 is used for the gyro.

$$G_{GYRO} = \frac{w_n^2}{s^2 + 2\xi w_n s + w_n^2}, w_n = 2 * \pi * f, f = 400, \xi = 0.707 \tag{16}$$

In the HEL testbed, the power amplifier utilizes its dual phase command mode. The phase inputs are sinusoidal and 120° out of phase from each other, while the third phase is internally generated by the amplifier. This configuration was chosen since it provides smooth motion while minimizing motor torque ripple proving maximum accuracy. The amplifier mathematical model can be thought of as an LPF, which has a -3dB bandwidth of 2KHz, and is expressed by:

$$G_{Power-AMP} = \frac{w_n^2}{s^2 + 2\xi w_n s + w_n^2}, w_n = 2 * \pi * f, f = 2000, \xi = 0.707 \tag{17}$$

Optics in Motion model OIM-101 FSM is used on the HEL testbed. These mirrors consist of a one-inch glass with a user-replaceable mirror/sub-mount where the mirror is hard mounted to the mirror gimbal. A built-in high precision optical sensor monitors mirror angles and provides feedback information to the internal controller. A scale factor of 10V = 1.5 degrees over a range of ±10V is used by the local position sensor. As previously discussed, frequency response testing showed the -3dB bandwidth of the closed position loop is 360Hz, meaning that the FSMs can be modeled as second order low pass filter (LPF) given by Equation 18.

$$G_{FSM} = \frac{w_n^2}{s^2 + 2\xi w_n s + w_n^2}, w_n = 2 * \pi * f, f = 360, \xi = 0.707 \tag{18}$$

A number of limit switches are included in the testbed to protect various components. See Table 5 for a summary of these limit switches.

Table 5.   Limit function summary [From 6]

Item	Limit Value	Unit
Voltage Limit	±10	Vdc
Current Limit	±10	A
Torque Limit	±23.9	N-m
Gyro Limit	±23.9	Deg/sec

Finally, a disturbance input model was also included in the Matlab/Simulink system model. For simplicity, an existing ground fighting vehicle model that expresses the disturbance as a power spectral density function was utilized, see Equation (19)19. The RMS disturbance value was 83mil/sec.

$$PSD = \frac{31.2*10^3 f}{(1+4f^2)^{3/2}} \cdot \frac{(mil/\sec)^2}{Hz}, 0.25 \le f \le 50Hz \tag{19}$$

2.   WFOV Control Loop

Using the components models developed in the previous section, the WFOV control loop, consisting of an inner and outer loop, was constructed as shown in Figure 39. The inner loop is a rate control loop, which provides stabilization with respect to external disturbances and tracking functions based on gyro feedback. The outer loop is an angular control loop that automatically maintains LOS to the target center based on WFOV camera feedback.
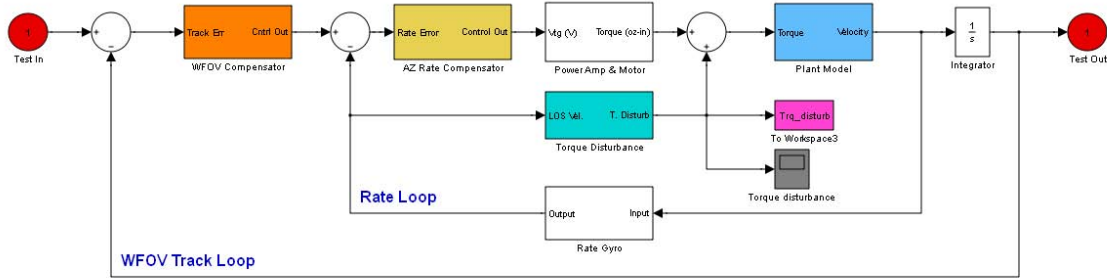
Figure 39.   WFOV Simulink model

a.   *Rate Control Loop*

The step response and corresponding transfer function can be seen in Figures 40 through 43. Bandwidth of the Matlab/Simulink model matches that of experimental results. The frequency response shows some deviation from experiment results, both at low frequencies and around the mechanical resonant frequency. This was due to the assumption of a simple linear model for the gimbals, which does not account for resonance or nonlinear effects.
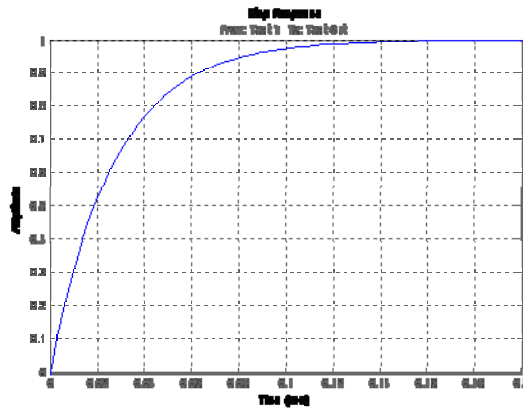
Figure 40.   Azimuth axis step response
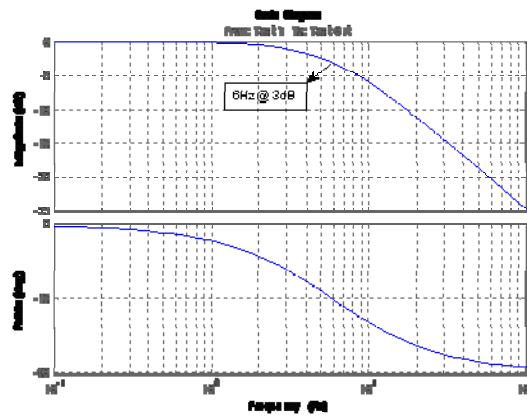
Figure 41.   Azimuth axis transfer function
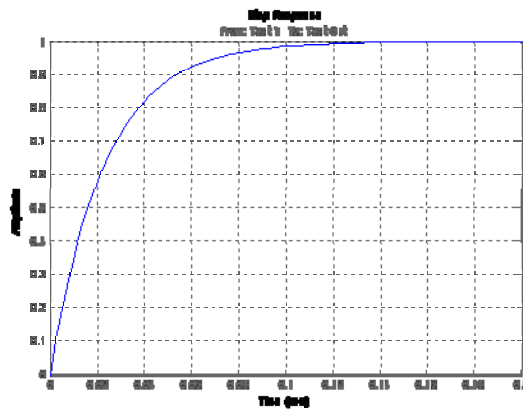
Figure 42.   Elevation axis step response
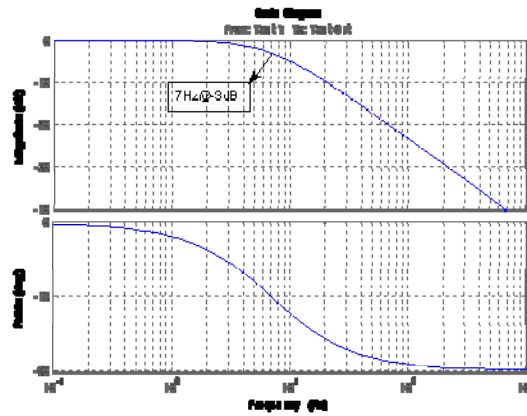
Figure 43.   Elevation axis transfer function

b.   *Position Control Loop*

Outer position loop simulation results are shown in Figures 44 through 47, while Table 6 contains a summary of model parameters and simulations results.
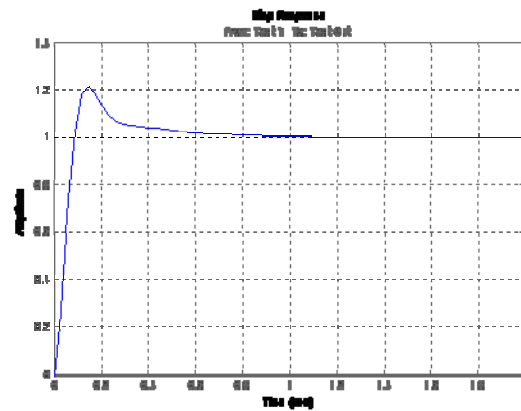
Figure 44.   Azimuth axis step response
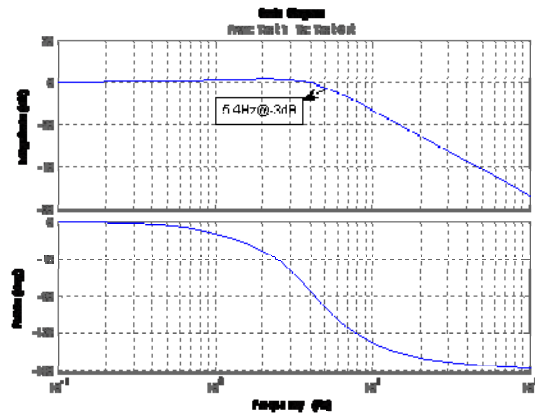
Figure 45.   Azimuth axis transfer function
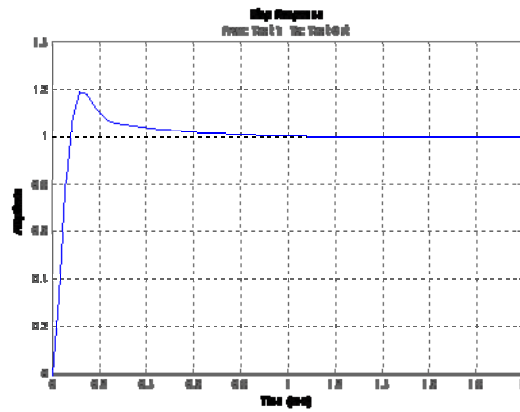
Figure 46.   Elevation axis step response
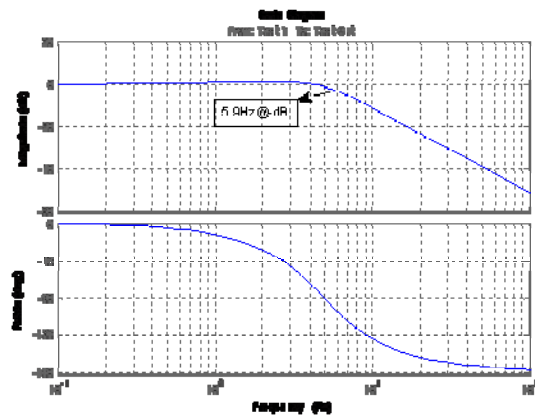
Figure 47.   Elevation axis transfer function

Table 6.   WFOV simulation parameters and results

Items		AZ axis	EL axis
Gimbal Inertia		1000 in-oz	260 in-oz
Rate loop	Compensator	94.4 (P-controller)	28.8 (P-controller)
	-3dB BW	6Hz	7Hz
WFOV position loop	Compensator (PI-controller)	$\dfrac{0.0063s + 0.01982}{s}$	$\dfrac{0.006918s + 0.02173}{s}$
	-3dB BW	5.4Hz	5.9Hz

3.   NFOV Control Loop

The model for the NFOV control loop is shown in Figure 48.   The FSM is modeled as a second-order system, as was verified through experimentation. Additionally, the NFOV control loop includes an integrator type compensator (on each axis) as summarized in Table 7. Simulation results for one axis are shown in Figures 49 and 50, since each axis has identical characteristics.   Finally, simulation bandwidth matched experimental results.
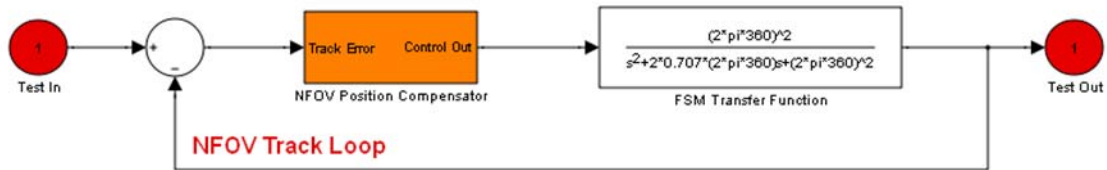
Figure 48.   NFOV Simulink model
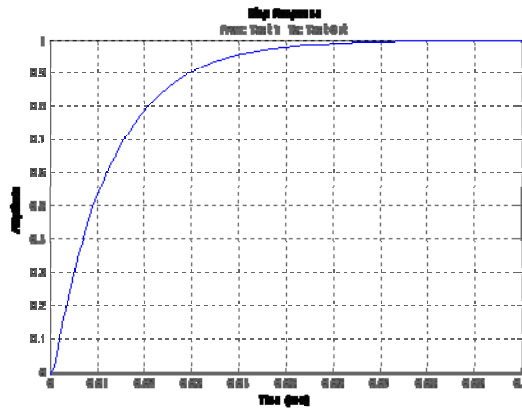
Figure 49.   NFOV step response
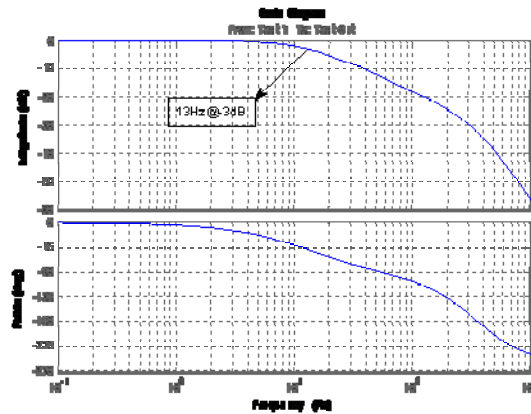
Figure 50.   NFOV frequency response

Table 7.   Summary of NFOV control loop model parameters

Items	AZ axis	EL axis
Compensator (I-controller)	$\dfrac{1.2388}{s}$	$\dfrac{1.2388}{s}$
-3dB BW	13Hz	13Hz

4.   **Integrated Control Model**

The WFOV and NFOV models were combined to create an integrated model of the HEL testbed (Figure 51). The WFOV block, containing an inner rate control loop and outer position control loop, is located in the lower portion of the integrated model. The upper portion of the model contains the NFOV track loop. Input to the NFOV loop is the track error generated by the WFOV track loop.

Figure 51.   Integrated HEL model

Two types of simulations were conducted with the integrated model. In the first test, target tracking performance of the model was evaluated, see Figures 52 through 55. Target motion was a sinusoidal with 2-degree peak at a frequency of 0.5Hz. At steady state, the WFOV has a peak track error of approximately 2.5mrads, and the NFOV has less than 0.1mrads of peak error.

Figure 52.   Target motion

41

Figure 53.   Rate of WFOV LOS
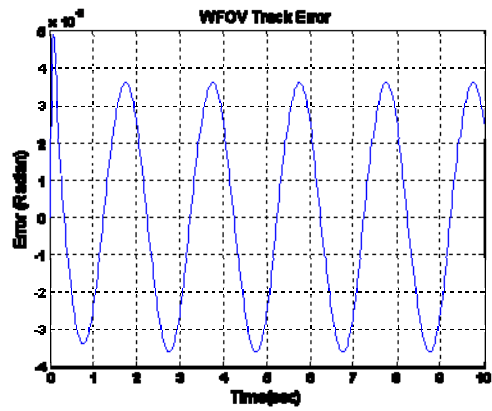
Figure 54.   WFOV track error
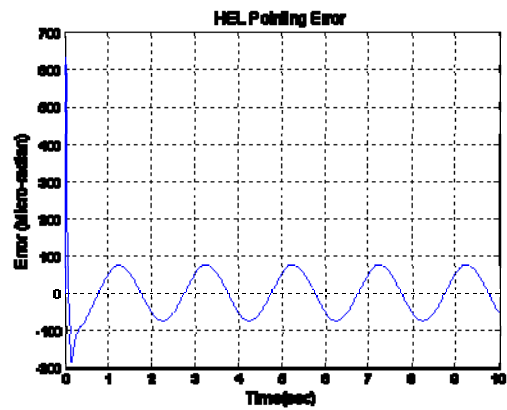
Figure 55.   NFOV track error

42

In the second test, disturbance rejection characteristics of the testbed were investigated, see Figures 56 through 59. The disturbance was a band limited random signal with 83mil/sec RMS, as described previously and shown in Figure 56. Peak error for the WFOV track loop increased to approximately 40 mrads, while NFOV track error increased to approximately 10 mrads, see Figures 58 and 59.
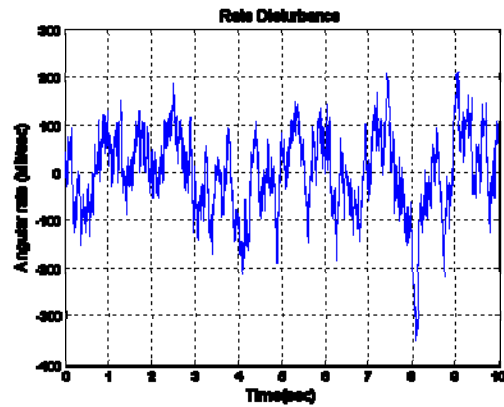
Figure 56.   Disturbance input
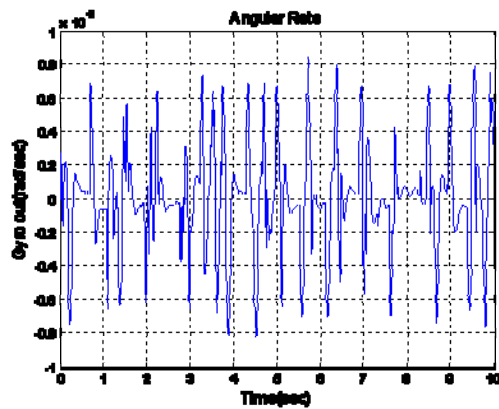
Figure 57.   Rate of WFOV LOS
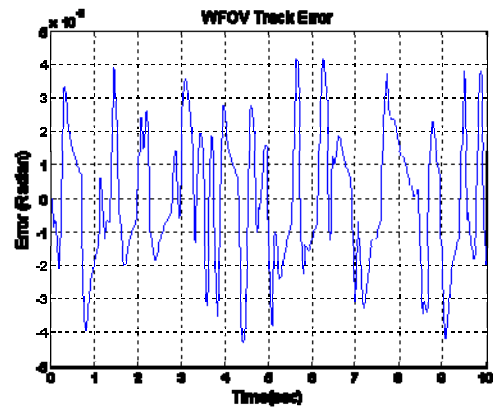
Figure 58.　　WFOV track error
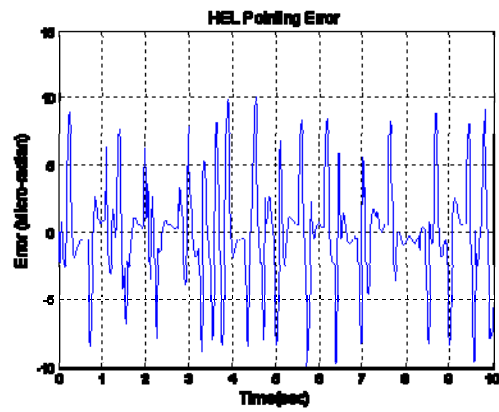
Figure 59.　　NFOV track error

IV.   CONTROL ALGORITHM IMPLEMENTATION

Two control algorithms were implemented on the HEL testbed. The first was an adaptive filter using the NFOV video tracker only. The second was an adaptive filter using a strapdown IRU, which consisted of a PSD, azimuth and elevation gyros and a reference laser. The NFOV Simulink model described in Chapter III was expanded to include multiple disturbance sources (mechanical vibration, atmospheric turbulence, etc.), as well as incorporating all three HEL testbed optical paths; incoming target image, reference laser, and surrogate kill laser; see Figure 60. The *Controller and Plant* subsystem of Figure 60 actually contains three separate controllers, shown in Figure 61. The first is the video tracker feedback loop, the second a gyro adaptive feedforward controller, and the final the PSD adaptive feedback controller. Both FX-LMS and FX-RLS algorithms were implemented for all three controllers. Most of the component models developed in Chapter III were used for this new model.
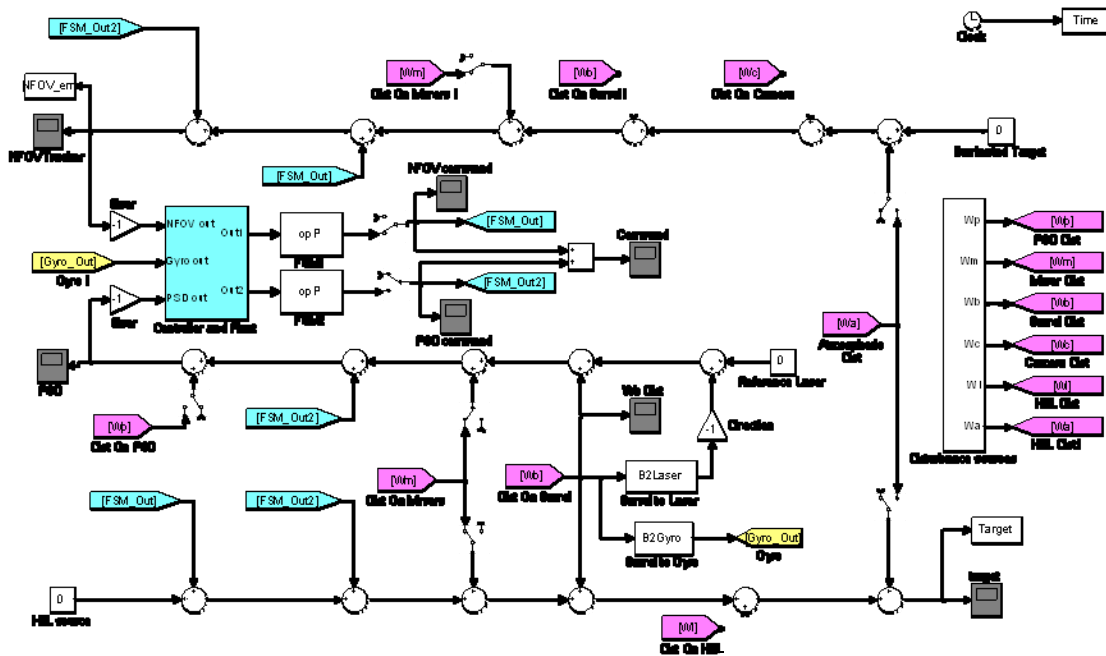
Figure 60.   NFOV Simulink model incorporating multiple disturbances
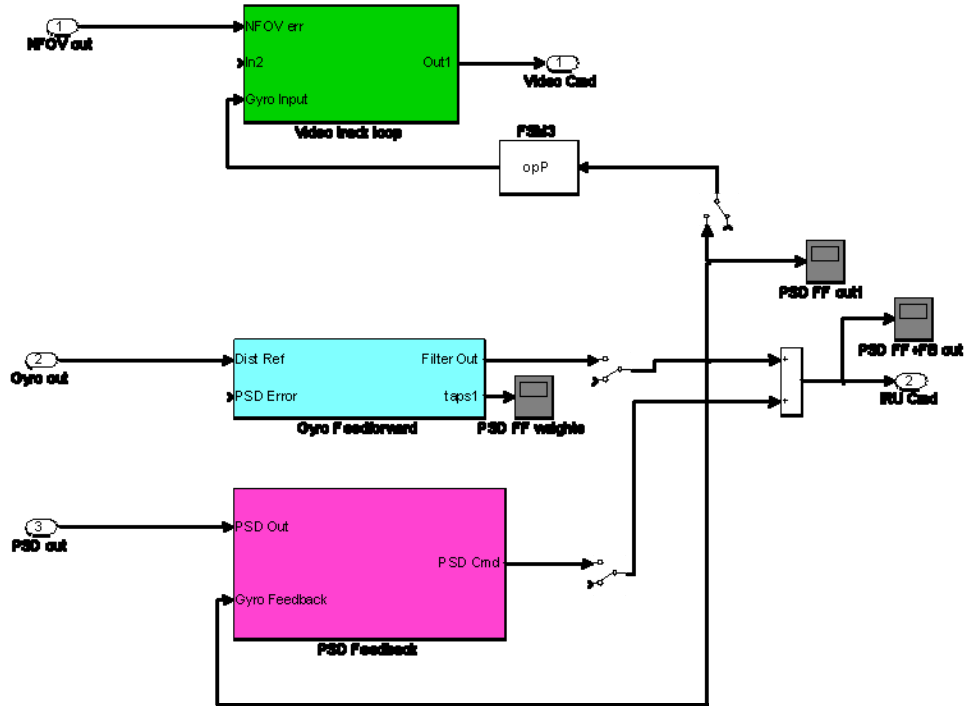
Figure 61.   NFOV control loops

A.   ADAPTIVE FILTER USING NFOV VIDEO TRACKER

Adaptive control was implemented on the NFOV using only the video tracker. This implementation was of the feedback type, as described in Section II.B, see Figure 4. The adaptive controller is in parallel with a fifth-order median filter (used to reject erroneous noise seen in experiments), and whose output is prior to the existing proportional-plus-integral (PI) controller, see Figure 62. Additionally, both FX-LMS and FX-RLS adaptive algorithms are implemented.
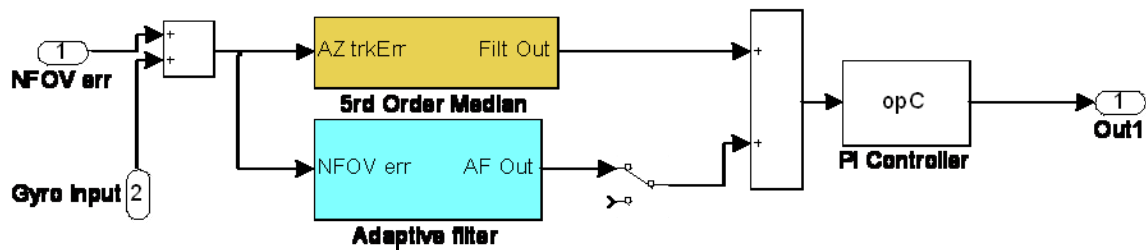
Figure 62.   Video tracking control loop

1.   Simulation Results

NFOV video tracker simulations were conducted with three disturbance sources. The first two were from mechanical vibration, one at 20 Hz and another at 50 Hz. The third disturbance was a 0.5 Hz sinusoidal in addition to broadband white noise. This was to simulate the effects of atmospheric distortion and target motion. Only the PI controller was active for the first two seconds of all simulations. A comparison of FX-LMS and FX-RLS performance is shown in Figures 63 through 65. The frequency analysis shown in Figures 63 and 64 was conducted on the steady state period of 9-12 seconds. As expected, there is a significant reduction in target error once the adaptive filter is engaged. Both LMS and RLS algorithms reduced RMS target error to less than one quarter of that produced by the PI controller alone. While the FX-RLS algorithm produces lower steady state error, it has the drawback of significant transient errors. The FX-LMS algorithm is much slower to converge. Further indication that FX-LMS is slower to converge can be seen in Figure 65, which illustrates the convergence of FX-LMS and FX-RLS weights. After ten seconds, FX-RLS weights have stabilized, while FX-LMS weights continue to change.
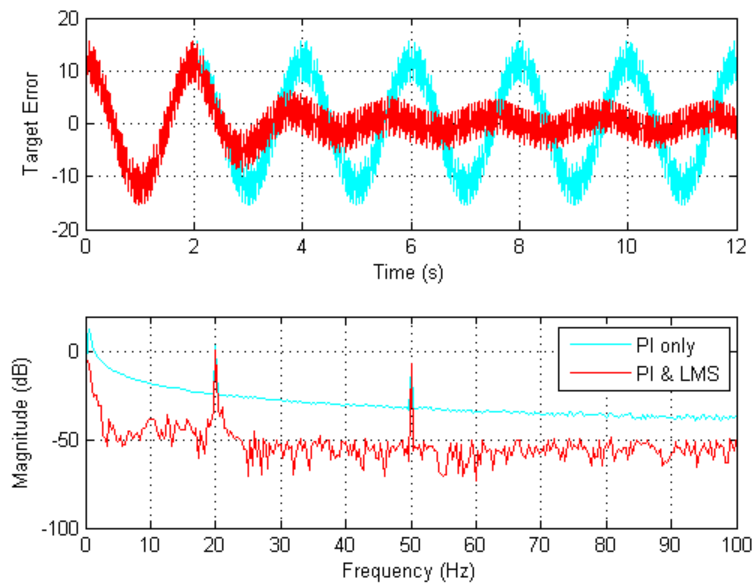
Figure 63.   Target error using NFOV FX-LMS controller
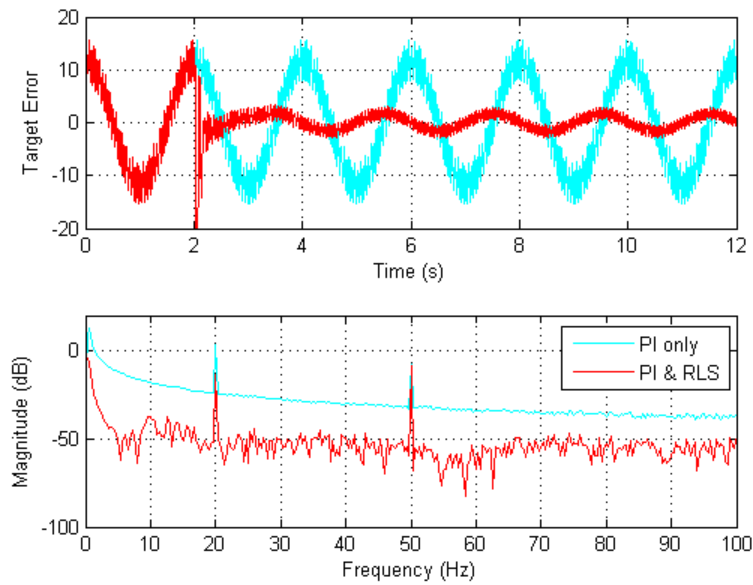
Figure 64.   Target error using NFOV FX-RLS controller
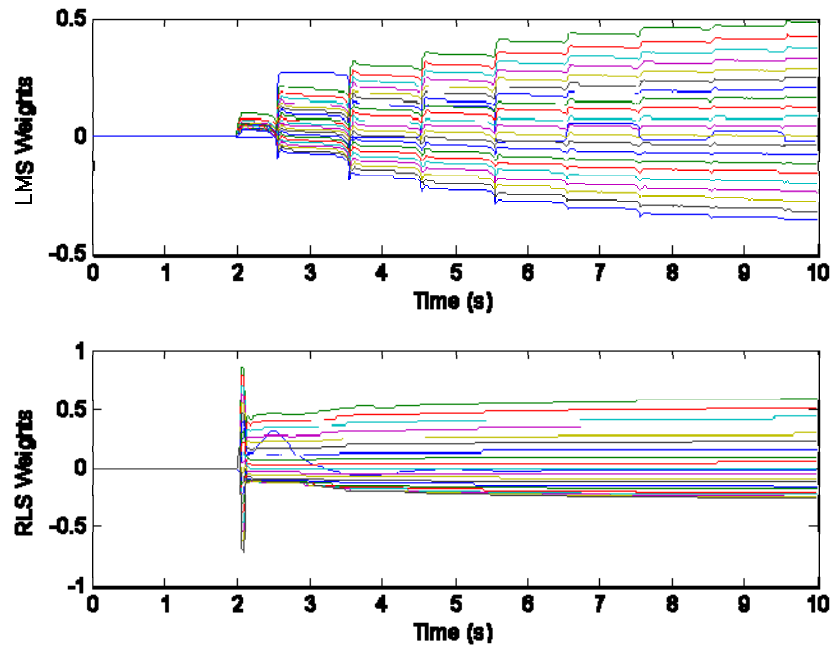
Figure 65.   Video tracker adaptive filter weight comparison

B.   ADAPTIVE FILTER USING IRU

Beam control contribution from the IRU consists of two adaptive filters in parallel, the adaptive feedforward control using gyros, and the adaptive feedback control using the PSD (Figure 61). The IRU is exclusively used to detect and correct platform vibration, it will not detect any atmospheric distortion. While the NFOV tracker also can detect vibration (sees it as target motion), significant errors can be introduced by the video tracking algorithm. Specifically, the video tracker uses a centroid computation to track the image. Since the image is not always clear, the NFOV video track loop may see errors in centroid calculations as target motion/platform vibration. The IRU is less susceptible to this problem since it uses a laser which travels much shorter distances than an image that is seen by the NFOV video tracker. Also, the optic path the reference laser follows is not subjected to any atmospheric distortion which aid in focusing it on the PSD.

The gyro adaptive controller was implemented using FX-RLS only, while the PSD controller was implemented using both FX-LMS and FX-RLS. The gyro

49

feedforward controller, Figure 66, uses the gyro signal as a reference and estimates the error. Specifically, the error is estimated as the difference in the gyro signal multiplied by the inverse of the transfer function between the gyro and disturbance, and the filter output multiplied by the transfer function of the FSM, see Equation 20. The PSD feedback controller (Figure 67) is similar to the video tracking adaptive filter, since both estimate the disturbance based on the error and filter output. As in the hybrid feedforward and feedback controller of [8], the PSD feedback controller error is the sum of the gyro feedforward output and the error from the PSD itself. The filter command calculated by both IRU controllers is summed and sent to the auto-alignment FSM.

$$error = G_{gyro}^{-1} g - G_{fsm} f$$
$$where:$$
$$g = \text{gyro signal}$$
$$G_{gyro} = \text{transfer function between disturbance and gyro}$$
$$f = \text{filtered output}$$
$$G_{fsm} = \text{FSM open loop transfer function}$$

(20)
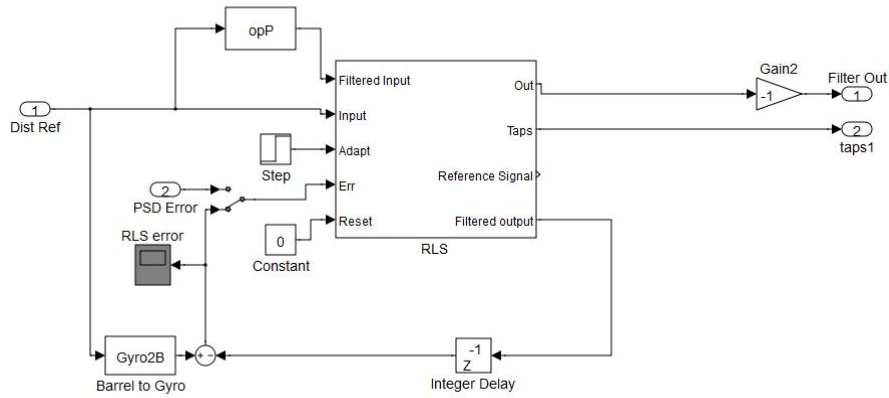
Figure 66.   Gyro feedforward adaptive controller
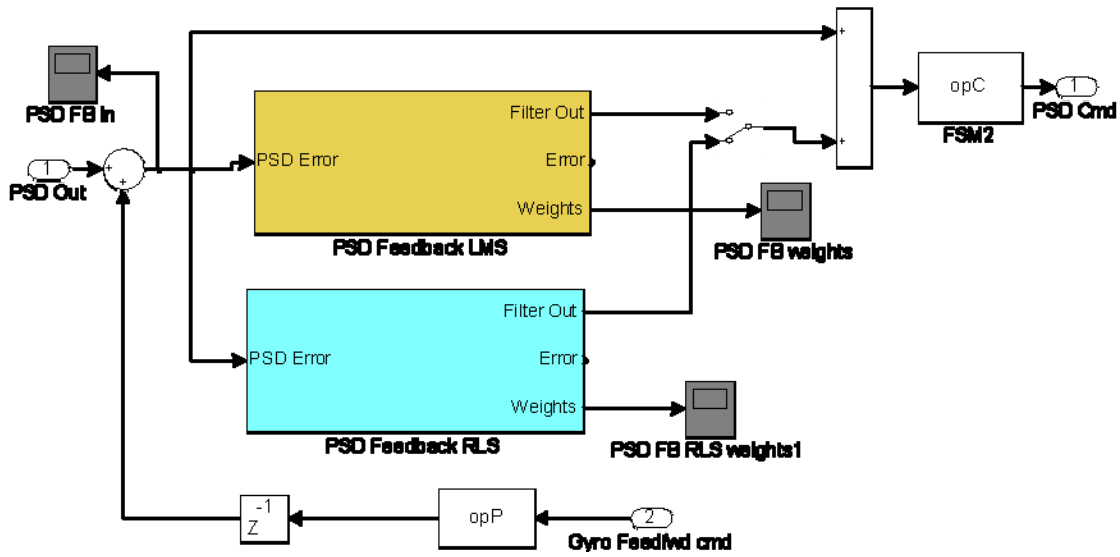
Figure 67.   PSD feedback adaptive controller

1.   Simulation Results

Simulations were conducted using the same 0.5 Hz, 20 Hz, and 50 Hz sinusoidal signals along with broadband white noise. Simulation results of the PI controller only, PI plus PSD adaptive feedback and PI plus PSD adaptive feedback along with gyro feedforward can be seen in Figures 68 and 69.   For both plots, the IRU adaptive filters are active after 4 seconds. The frequency analysis is from the steady state period of 9-12 seconds. Using the adaptive feedback controller combined with the feedforward adaptive controller using the gyros results in an RMS error of 0.083 for the LMS algorithm and 0.073 for the RLS algorithm. Additionally, the feedforward controller is able to reduce the 20 Hz disturbance, which the PSD feedback filter cannot effect (since it is unable to detect rigid body motion).

51
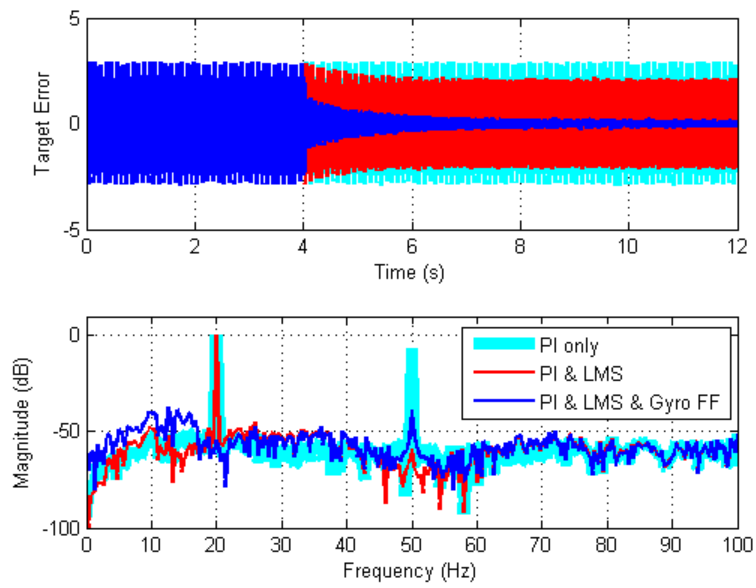
Figure 68.　　　IRU effectiveness using FX-LMS Algorithm
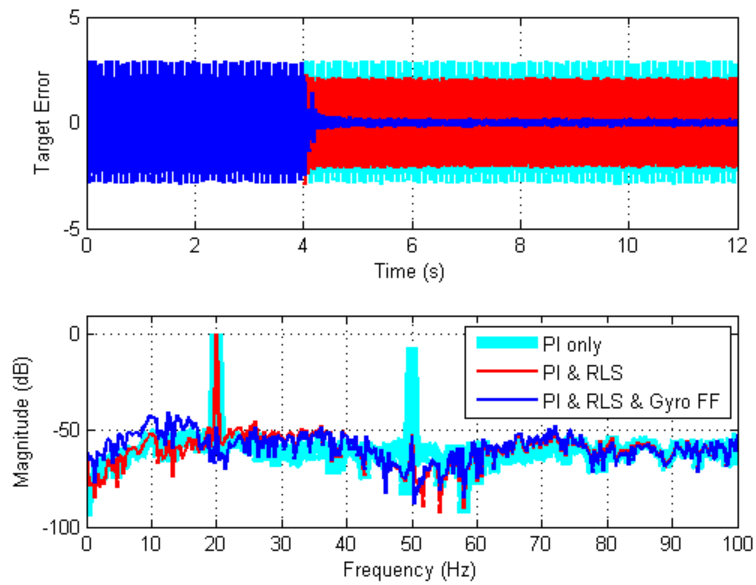
Figure 69.　　　IRU effectiveness using FX-RLS algorithm

V. EXPERIMENTAL RESULTS

The adaptive controllers from Chapter IV were implemented on the HEL testbed and experiments were conducted to evaluate their performance. In all experiments, the disturbance is a 0.5 Hz sinusoidal signal sent to the disturbance FSM. This disturbance affects all three optical paths. Disturbance magnitude was 800 mV. Other natural disturbance sources include the power amplifiers, gyros and gimbals. It is assumed atmospheric disturbances are negligible.

A. STABILITY ISSUES

When the FX-LMS adaptive filter was implemented in the NFOV tracking algorithm of the HEL testbed, stability issues arose. After approximately 10 seconds, the system would become unstable and lose track of the incoming target image. It was determined that the stability issues was caused by an incorrect model identification of the PI-Control closed loop system. The more accurate plant model is 5th order (first order controller, second order FSM and second order track sensor). Figure 70 illustrates the differences in frequency response for the two models. The old plant model has a significant phase difference above 10 Hz, which is the most likely cause of instability. Simulations were also conducted with the updated plant, see Figure 71.
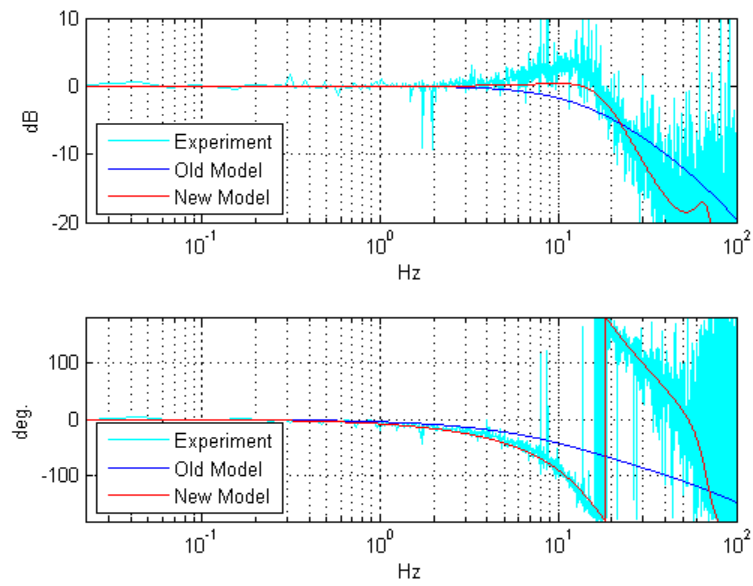
Figure 70.   Bode plot for original and new plant models
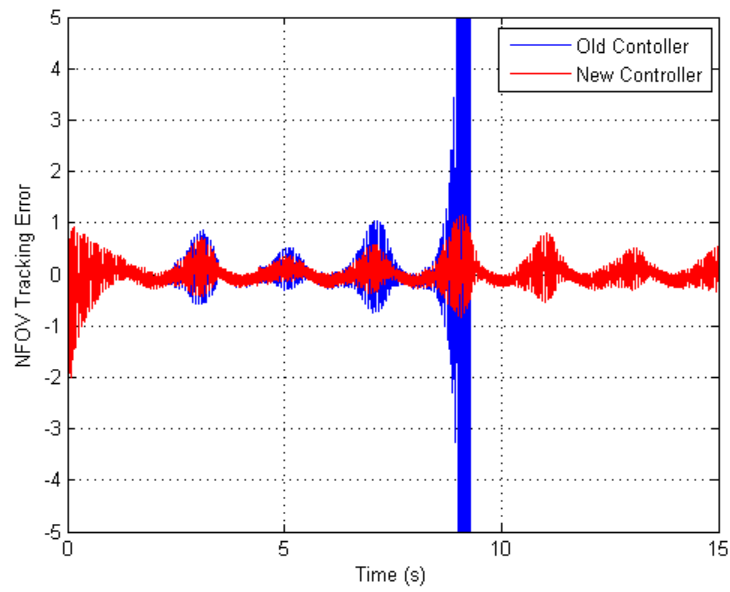
Figure 71.   Simulation comparison of old and new plant models

B.   ADAPTIVE FILTER USING NFOV VIDEO TRACKER

Once the stability issues of Section A were identified and corrected, FX-LMS and FX-RLS algorithms were implemented on the NFOV track loop. FX-LMS experimental results are shown in Figures 72 and 73. In this case, the NFOV adaptive filter is active after approximately 35 seconds. At the disturbance frequency of 0.5 Hz, NFOV track error was reduced by approximately 18 dB. FX-RLS experimental results are shown in Figures 74 and 75, and for this test the adaptive filter is active after approximately 35 seconds. NFOV error was reduced by approximately 19 dB at the 0.5 Hz disturbance frequency when using the FX-RLS algorithm.
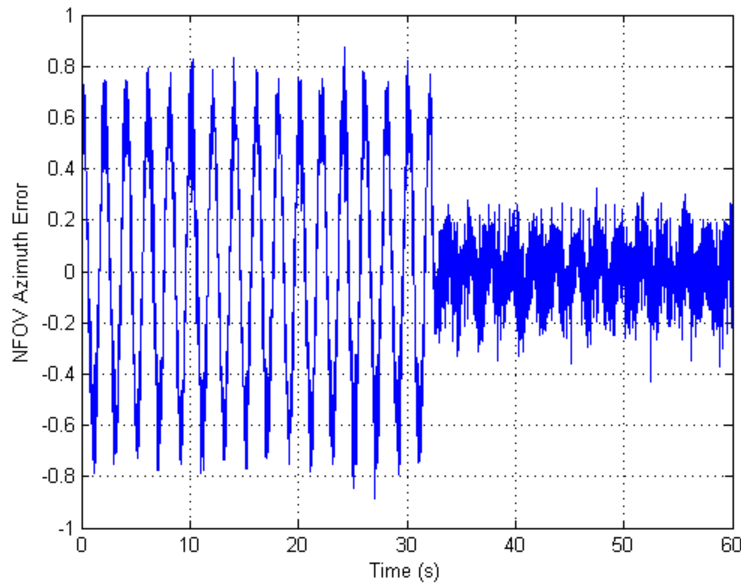
Figure 72.   NFOV track error, FX-LMS algorithm
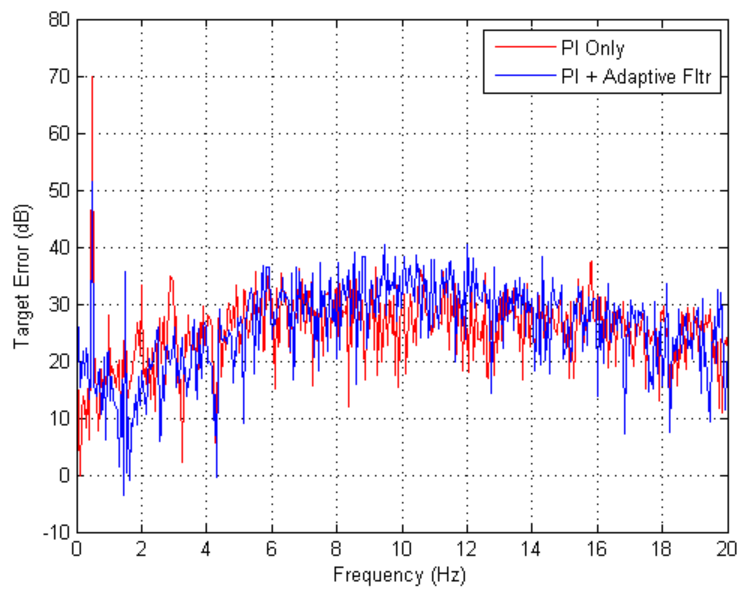
Figure 73. Frequency domain NFOV track error, FX-LMS algorithm
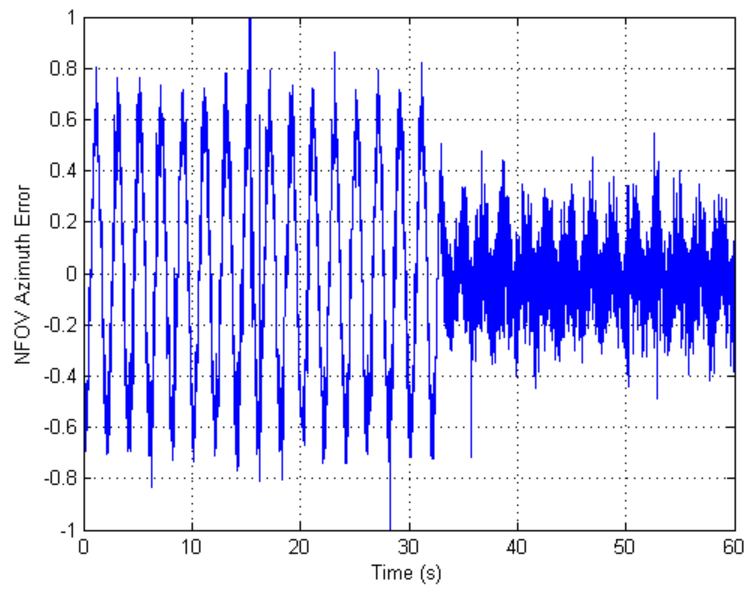
Figure 74. NFOV track error, FX-RLS algorithm
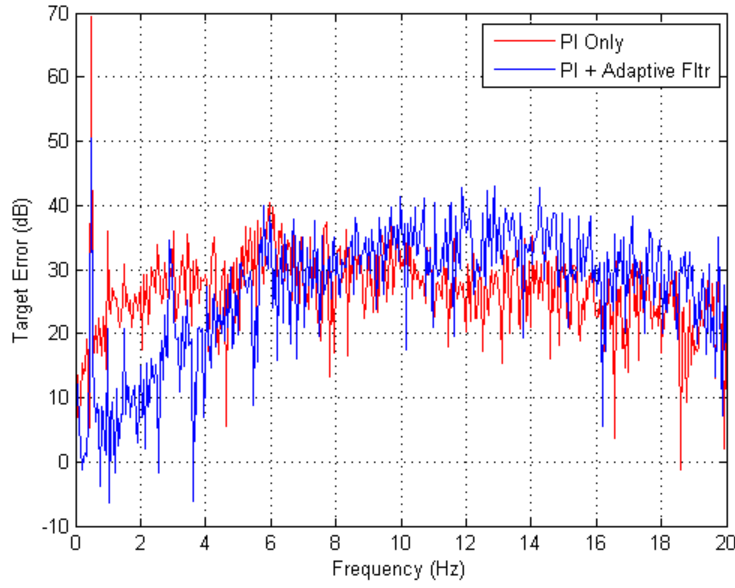
Figure 75.   Frequency domain NFOV track error, FX-RLS algorithm

C.   FEEDFORWARD ADAPTIVE CONTROL USING GYROS

Prior to implementing a strapdown type IRU, a demonstration was conducted using the elevation gimbal gyro in a feedforward signal. To accomplish this, the transfer function between the gyro and the FSM was required. This transfer function was developed using two tests, the first to determine the transfer function between the error at the PSD and the gyro output and the second a transfer function between the FSM output and the error at the PSD. Disturbance motion in both tests was detected by the PSD. This transfer function is summarized in equations 20 through 22 where y_{psd} is the error measured at the PSD, G_g is the transfer function between the gyro and the PSD, g is the gyro signal, G_{FSM} is the transfer function between the FSM and PSD and u is the control signal to the FSM. Testing in Chapter III already determined the FSM could be modeled as a second order LPF (Equation 18). A system identification was conducted to determine G_g, which is a first order transfer function (Equation 23).

$$y_{psd} = G_g g \tag{21}$$

$$y_{psd} = -G_{FSM} u \tag{22}$$

$$u = -\frac{G_g}{G_{FSM}} g \tag{23}$$

$$G_g = \frac{1}{s + \tau}; \quad \tau = 1.6 \tag{24}$$

Since this was only a demonstration of the feasibility of using gyro feedforward control, the disturbance was limited to 5 Hz. The gains for both G_g and G_{FSM} were optimized for 5 Hz.

Experimental results for the gyro feedforward controller can be seen in Figures 76 and 77. The 5 Hz disturbance was turned on just prior to 3 seconds, and the feedforward controller was turned on after 6 seconds. It should be noted there was a boresight error, which caused the target error to be non-zero prior to application of the disturbance. By using the gyro feedforward controller, target error at the disturbance frequency of 5 Hz was reduced by approximately 8 dB. Calibration of the system could produce further error reductions but was not attempted since these experiments were meant to simply demonstrate the feasibility of use the gyro signal in a feedforward controller.
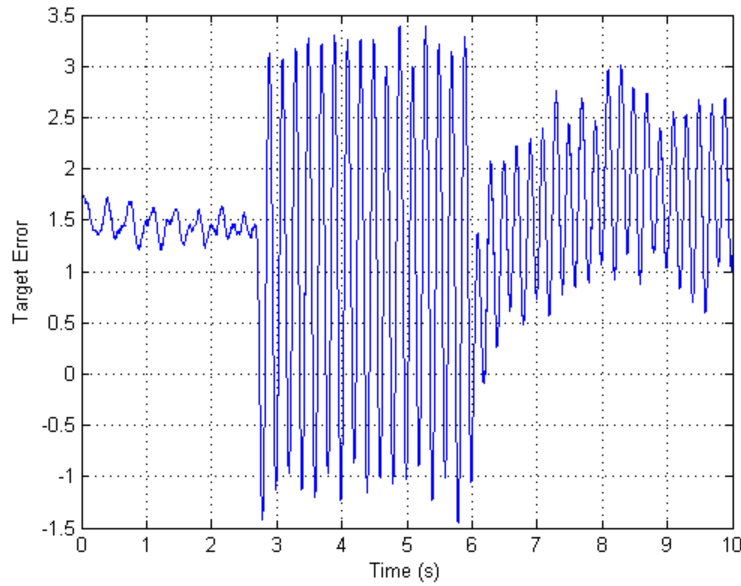
Figure 76.   Time domain gyro feedforward results
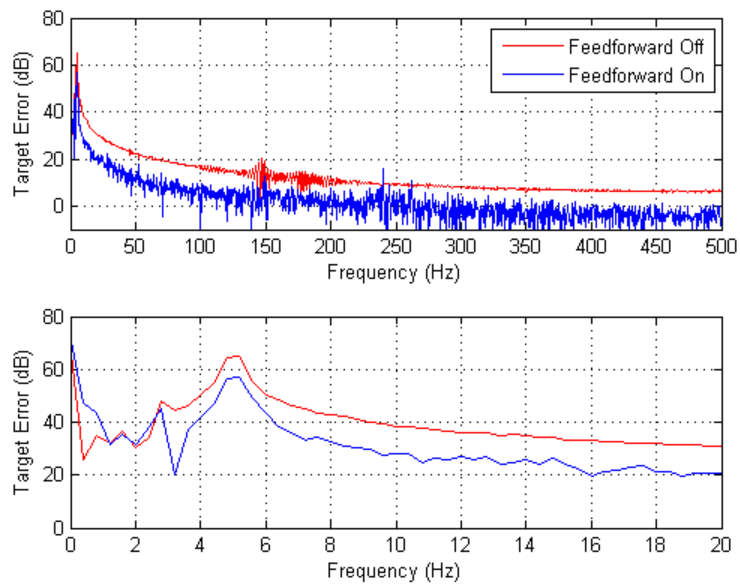
Figure 77.   Frequency domain gyro feedforward results

THIS PAGE INTENTIONALLY LEFT BLANK

VI. CONCLUSION

A. SUMMARY

While not directly related to, the research of this thesis drew on much of the work in beam jitter control accomplished previously at NPS by Professor Brij Agrawal, Dr. Joseph Watkins, Brett Bateman, Michael Beerer and Dr. Hyungjoon Yoon [8], [10], [12]. In their research, feedforward and feedback adaptive filters using multiple reference sources were implemented on the jitter control testbed (JCT). The purpose of this research was to implement those beam jitter control techniques onto the HEL testbed.

A basic system characterization of the HEL testbed was required prior to implementation of any adaptive controllers were implemented. This characterization resulted in the development of Matlab Simulink models, which proved extremely useful in developing and testing new control methods. Adaptive filters using the FX-LMS and FX-RLS algorithms were simulated for the NFOV video tracker. Additionally, simulations were conducted using an IRU for a hybrid adaptive controller. This controller contained a feedback adaptive filter using a signal from the PSD and a feedforward adaptive filter using a signal from the gyros.

Both FX-LMS and FX-RLS algorithms were implemented on the NFOV video track loop of the HEL testbed. Experiments results show significant reduction in track error, especially at the disturbance frequency. As a prelude to implementation of the IRU hybrid adaptive controller, a simple gyro feedforward controller was implemented on the elevation axis of the HEL testbed.

B. FUTURE WORK

In Chapter V, a gyro feedforward controller was added to the HEL testbed. The next step is to fully implement the strapdown IRU and associated adaptive controllers, which were simulated in Chapter IV. Currently though, the gyro feedforward controller uses the gimbal gyro, which is located at the base of the telescope. A better solution is to add additional gyros at the tip of the telescope, which are co-located with the reference laser.

Additional work would be to develop a more accurate transfer function between the gyros and the FSM. This could be accomplished by performing tests in which the loop is closed and error measurements are taken from a target PSD. A more accurate transfer function would allow the gyro feedforward controller to perform better over a wider range of frequencies, rather than being tuned for a single frequency, as is currently the case.

Finally, this research concentrated solely on implementation of adaptive filter controllers for tracking a static target. Actual HEL systems, such as ABL and ATL must also have the ability to track a moving target. The WFOV mode of the HEL testbed allows it to track moving targets, but the ability of the NFOV track loop to maintain lock on a moving target is limited. At the present time, not work has been conducted on combining the WFOV and NFOV control loops would could increase the ability of the NFOV to maintain lock of a moving target.

APPENDIX: EQUIPMENT SPECIFICATIONS

A.   ON-TRAK OT-301 POSITION SENSING DEVICE

Table 8.   ON-TRAK OT-301 PSD specifications

Transimpedance Gain (V/A) Four input channels	4×10^6 to 4×10^3 (Six Ranges)
Input Current Range	1.5 μA to 1.5 mA
Output Voltage: -position X,Y -Sum	+/- 10V 0-6 V
Zero Offset (Offset Null)	+/- 1 V Each Axis
Calibration Adjust	+/- 10% Full Scale (+/- 1V)
Detector Bias	0 V, +/- 5 V
Frequency Response	DC to 15 kHz (range dependent) G1 16 kHz G2 16 kHz G3 5 kHz G4 1.25 kHz G5 310 Hz G6 80 Hz
Output Connectors	BNC
Input Connectors	Sub Min. DB9 female receptacle
Power Requirements	12V, 500 mA (AC Adapter)
Dimensions	5.57 x 1.52 x 6.00 inches

B. IMPERX IPX VGA 210-L VIDEO CAMERA

Table 9.   IPX VGA 210-L video camera

CCD sensor	KAI-0340S/D
Pixel size	7.4 μ m
Black rows – top	4
Buffer rows – top	4
Active rows – (V)	480
Buffer rows – bottom	4
Black rows – bottom	0
Dummy pixels – left	12
Black columns – left	24
Buffer columns – left	4
Active pixels – (H)	640
Buffer columns – right	4
Black columns – right	24
Dummy pixels – right	12
Frame rate – single	120 fps
Frame rate – duale	210 fps

C. KVH DSP-3000 FIBER OPTIC GYRO

KVH Industries DSP-3000 series fiber optic gyro, part no 02-1222-02 digital, 1 kHz synchronous gyro.

Table 2: Product Specifications

Attribute	Rating	
Performance		
	Digital	**Analog**
Maximum Input Rate	±375°/sec	±100°/sec
Scale Factor		
Linearity (room temp)	1000 ppm, 1σ of full scale, for ±375°/sec	500 ppm, 1σ of full scale
	500 ppm, 1σ of full scale, for ±150°/sec	
Temperature Sensitivity	500 ppm, 1σ	500 ppm, 1σ
Error (full rate & temp)	1500 ppm, 1σ	1000 ppm, 1σ
Bias		
Offset (room temp)	±20°/hr	±100°/hr
Stability (room temp)*	1°/hr, 1σ	3°/hr, 1σ
Temperature Sensitivity (<1°C/min)	6°/hr, 1σ	20°/hr, 1σ
Bandwidth (3 dB)	>40 Hz, 100 Hz asynchronous	100 Hz
	>400 Hz, 1000 Hz synchronous or asynchronous	
Update Rate	100/sec, 100 Hz asynchronous	2000/sec
	1000/sec, 1000 Hz synchronous or asynchronous	
Angle Random Walk (noise)*	4°/hr/√Hz 0.0667°/√hr	6°/hr/√Hz 0.1°/√hr
Initialization Time (valid data)	<5 sec	

* Bias Stability and Angle Random Walk determined by Allan variance method.

Figure 78.   KVH DSP-3000 fiber optic gyro specification, part 1

Table 2: Product Specifications (Continued)

Attribute	Rating	
Electrical		
	Digital	**Analog**
Input Voltage	+5 VDC ±10%	
Power Consumption	3 watts maximum (2 watts typical)	
Output		
Type	38,400 Baud (RS-232), 100 Hz asynchronous	±2 VDC full scale, differential
	115,200 Baud (RS-232), 1000 Hz asynchronous	±1 VDC full scale, single-ended
	3.072 MHz serial, 1000 Hz synchronous	
Format (selectable)	Rate, Incremental Angle, or Integrated Angle	Rate
Physical		
Dimensions	3.5" x 2.3" x 1.3" (88.9 mm x 58.42 mm x 33.02 mm)	
Weight	0.6 lbs (0.27 kg)	
Environmental		
Operating Temperature	-40°F to +167°F (-40°C to +75°C)	
Storage Temperature	-58°F to +185°F (-50°C to +85°C)	
Shock (functional)	Functional sawtooth 40 g, 6-10 msec	
Random Vibration	20 to 2000 Hz, 8 g rms, operational	
MTBF	>55,000 hours, ground mobile	

⚠ In all cases while operating, input rate must not exceed ±500°/second. If the input rate exceeds ±500°/second, physical damage will not occur but the output data will become unreliable, regardless of the validity BIT.

Figure 79. KVH DSP-3000 fiber optic gyro specification, part 2

D. OPTICS IN MOTION OIM101 FSM

Table 10. OIM101 FSM specifications

Mirror size	1 in x 0.25 in
Wave-front quality	1/10 wave p-v
Useable aperture	0.94 in
Scale factor	10 V = 1.5 deg (26.2 mrad)
Range	+/- 10 V
Power	+/- 15 V, 1.5 A

THIS PAGE INTENTIONALLY LEFT BLANK

LIST OF REFERENCES

[1]   D. Lamberson, E. Duff, D. Washburn, and C. Holmberg, "Whither High-Energy Lasers?," *Air and Space Power Journal*, vol. XVIII, no. 1, pp. 15–24, 2004.

[2]   J. Skillings. (2009, Oct.) CNET News. http://news.cnet.com/cutting-edge/8300-11386_3-76.html?keyword=Advanced+Tactical+Laser (accessed November 2, 2009).

[3]   "The Airborne Laser," Missile Defense Agency Fact Sheet, 2009.

[4]   P. Orzechowski, N. Chen, S. Gibson, and T.-C. Tsao, "Adaptive Control of Jitter in a Laser Beam Pointing System," in *Proceedings of the American Control Conference*, Minneapolis, MN, USA, June 2006, pp. 2700–2705.

[5]   S. M. Kuo and D. R. Morgan, "Active Noise Control: A Tutorial Review," *Proceedings of the IEEE*, vol. 87, no. 6, pp. 943–973, June 1999.

[6]   D. Kim, D. Frist, J. J. Kim, and B. Agrawal, "A HEL Testbed for High Accuracy Beam Pointing and Control," Naval Postgraduate School, Monterey, CA, Technical Report, 2009.

[7]   S. M. Kuo and D. R. Morgan, *Active Noise Control Systems: Algorithms and DSP Implementations*. New York: Wiley-Interscience, 1996.

[8]   M. Beerer, "Adaptive Filter Techniques for Optical Beam Jitter Control and Target Tracking," Master's thesis, Naval Postgraduate School, Monterey, CA, 2008.

[9]   S. Haykin, *Adaptive Filter Theory*, 4th ed. Upper Saddle River, New Jersey: Prentice Hall, 2002.

[10]   R. J. Watkin, "The adaptive control of optical beam jitter," Ph.D. disssertation, Naval Postgraduate School, Monterey, CA, Dec. 2004.

[11]   R. J. Watkins and B. N. Agrawal, "Use of least means squares filter in control of optical beam jitter,S" *Journal of Guidance, Control and Dyanamics*, vol. 30, no. 4, pp. 1116–1122, Jul. 2007.

[12]   B. E. Bateman, "Experiments on laser beam jitter control with applications to a shipboard free electron laser," Master's thesis, Naval Postgraduate School, Monterey, CA, December 2007.

[13]   S. Baugh, "Precision LOS Stabilization," SVS Inc, 1997.

THIS PAGE INTENTIONALLY LEFT BLANK

INITIAL DISTRIBUTION LIST

1. Defense Technical Information Center
    Ft. Belvoir, Virginia

2. Dudley Knox Library
    Naval Postgraduate School
    Monterey, California

3. Dr. Brij Agrawal
    Naval Postgraduate School
    Monterey, California

4. Dr. Jae Jun Kim
    Naval Postgraduate School
    Monterey, California

5. Dr. Masaki Nagashima
    Naval Postgraduate School
    Monterey, California